On the Neck-Like Deformation in High-Speed Spun Polyamides*

H. HABERKORN,† K. HAHN, H. BREUER, H.-D. DORRER, and P. MATTHIES

BASF AG, Polymers Laboratory, and Fiber Intermediates Division, Ludwigshafen, Germany

SYNOPSIS

The neck-like deformation process occurring in high-speed melt spinning of polyamide 66 and polyamide 6 filaments was investigated at take-up speeds of 4200 to 5500 m/min by on-line laser light scattering, thermographic contrast compensation, and wide-angle X-ray scattering (WAXS) measurements. New information about the onset of crystallization along the spinline was obtained by measuring simultaneously diameter and temperature profiles in the neighborhood of the neck. Crystallization rates, as a function of take-up speed, are estimated for both polyamides. Based on the present experimental results of diameter profiles, temperature profiles, and WAXS patterns, a picture of the physical mechanism responsible for the neck-like deformation of high-speed melt spun polyamides is proposed. © 1993 John Wiley & Sons, Inc.

INTRODUCTION

High-speed melt spinning of polycondensates is associated with a concentrated deformation process occurring immediately above the solidification point of the filament. As this process somewhat resembles the necking process observed in the cold drawing of polymers, it is often referred to as a "neck"-like deformation. Since the work of Perez and Lecluse,[1] who first reported on the formation of a neck-like deformation in high-speed spun polyethylene terephthalate (PET), necking has been observed independently by many authors, not only for polycondensates, but also for other crystallizing polymers.[2-14]

Thus far, necking has not been observed for non-crystallizing polymers. Therefore, it is generally believed that the occurrence of a neck-like deformation in high-speed spinning is somehow related to the crystallization process. However, this relationship is not yet understood. It is still an open question as to whether the neck-like deformation is initiated by the onset of crystallization, or if, for instance, crystallization is simply needed to prevent the filament from breaking under the strong stress increase during the concentrated deformation process in the neck. For amorphous polymers, a similar strong stress increase would result in fiber rupturing, making it impossible to observe the necking process experimentally.

Although the mechanisms involved in the necking process have not been clearly understood until now, there have been several attempts to describe the necking behavior by simple mathematical models.[8,13,15-17] Due to a lack of information, however, several arbitrary assumptions had to be made by the authors for these calculations. For example, with a semiempirical model, Schöne[15] was able to reproduce a neck-like deformation without taking into account a crystallization process. On the other hand, simulations allowing for an orientation-induced crystallization[8,13] were not successful in revealing the abrupt, neck-like deformation along the spinline.

In the present work, some results are reported that were obtained during high-speed melt spinning of polyamide 66 (PA 66) and polyamide 6 (PA 6) filaments at take-up speeds of 4200 to 5500 m/min. Diameter profiles and temperature profiles, as well as the development of the filament structure, were measured on-line by means of laser light scattering, thermographic contrast compensation, and WAXS

* Presented in part at the "Hamburg Macromolecular Symposium 1990" Hamburg, Germany, 26–28 September 1990.
† To whom correspondence should be addressed.

Journal of Applied Polymer Science, Vol. 47, 1551–1579 (1993)
 CCC 0021-8995/93/091551-29

film patterns, respectively. New information about the onset of crystallization along the spin line was obtained by measuring simultaneously diameter and temperature profiles in the neighborhood of the neck. Based on the present experimental results, a picture of the physical mechanism responsible for the neck-like deformation process in high-speed melt spun polyamide filaments is proposed.

EXPERIMENTAL

Materials

PA 6 filaments of two different molecular masses and PA 66 filaments were spun and investigated in this study. The relative viscosities η_r and the number average molecular masses M_n of the spun filaments are listed in Table I. In the following, the PA 6 fiber with the lower molecular mass is called PA 6-I and the polymer with the higher M_n is designated as PA 6-II. The relative viscosities were determined in a 1% solution of the polymer in concentrated sulfuric acid (96%) and the molecular masses were determined by analyzing the amount of endgroups. The approximation $M_w/M_n = 2$ can be assumed for both polyamides. All products contained 0.3% by weight TiO_2.

High-Speed Spinning

Figure 1 shows a schematic representation of the spinning equipment. Spinnerets with seven round holes were used, the single orifice being 0.025 cm in diameter and 0.05 cm in length. The spinning temperature was 278°C for PA 6-I, 288°C for PA 6-II, and 297°C for PA 66. The spinline was cooled with cross-flow air at 25°C and about 0.4 m/s. The mass throughput per orifice, $\dot{m}$, was in the range 1.4 to 2.3 g/min, that is, 10 to 16 g/min per spinneret.

On-Line Measurements

Filament Diameter

The filament diameter was measured without contact with laser light scattering (LLS) methods.[18,19] The laser beam was spherically and cylindrically widened to produce a beam with a line-like shape of a length of about 4 cm. The beam was focused on the running filament in the blowing duct. The diffraction pattern, scattered in the forward direction, was recorded with a CCD camera. Typical interference patterns, taken at different distances H from the spinneret, are shown in Figure 2.

Table I Relative Viscosities η_r and Molecular Masses M_n of PA 66 and PA 6 Filaments Under Investigation

PA	η_r	M_n
66	2.58	14600
6-I	2.60	15800
6-II	2.89	18800

The filament diameter D was determined from the distances between the interference maxima. The inclination of the interference stripes was proportional to the rate of diameter reduction dD/dH along the spinline. For filament diameters $D = 20$ μm, the factor of proportionality is about 2×10^4. This means that the inclination of the interference stripes is a powerful tool in order to determine the solidification point H'_o, which is defined as that distance from the spinneret where the filament diameter does not change any longer. Even reduction rates of dD/dH as small as 4×10^{-6}, corresponding to a reduction of the filament diameter by 1 μm over a length of 25 cm, would still show up as an angle of inclination of the interference stripes of 5 degrees.

The evaluation of the interference patterns was carried out fully automatically on an IBAS I+II image analyzer. Above the neck, filament diameters D, determined from different interference patterns, agreed well with each other ($\Delta D/D < 0.05$). In this region, three interference patterns were evaluated for each distance H. Their mean value $D(H)$ was used for the determination of the diameter profiles.

In the neck region, significantly larger diameter variations were obtained when evaluating different interference patterns. The position of H'_o was found to fluctuate by about ±2 cm around a mean value H_o. At distances close to H_o, interference patterns of a filament still in the melt state and those of a filament already solidified were observed. Therefore, in this region, mean values $D(H)$ of at least 6 single measurements of the filament diameter were used to create the diameter profiles.

Filament Temperature

The filament temperature along the spinline was measured with an infrared camera (AGA, Thermovision 782), using the contrast compensation method described in detail in Ref. 20. With this procedure, the threadline temperature is obtained by comparing the IR radiation emitted by the running filament with that of a reference heat source, the temperature of which is adjustable and well-known.

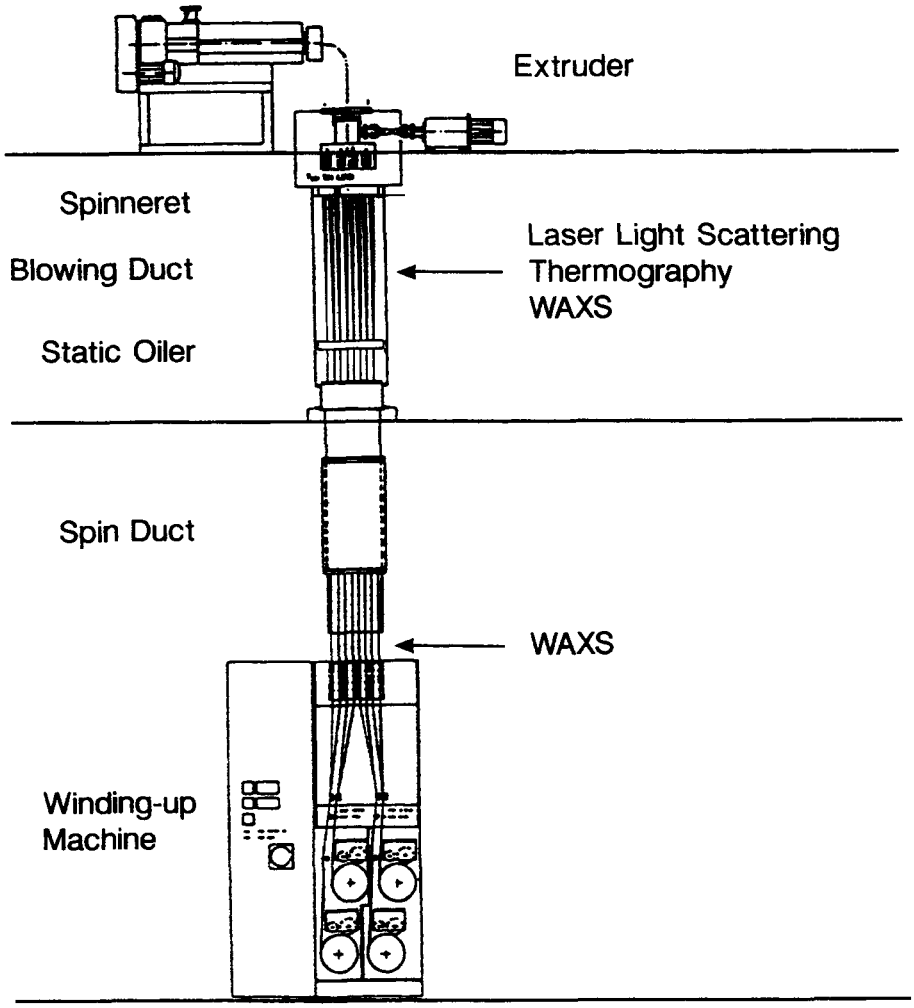

Figure 1 Schematic drawing of the high-speed spinning equipment indicating the positions of the on-line setups for laser light scattering, thermography, and WAXS.

For experimental convenience, the temperature and diameter measurements were carried out at two different filaments from the same thread, unless otherwise stated.

Filament Structure

The development of the filament structure was studied by means of wide-angle X-ray scattering (WAXS) measurements, applying the flat-film transmission technique. A Laue-type camera (HUBER) was mounted on a X-ray tube by a special mounting support. The X-ray tube itself was attached to an adjusting device movable parallel and perpendicularly to the draw-down direction. In order to reduce process-inherent lateral filament oscillations, a thread guide was mounted as close as possible to the transmission spot of the primary X-ray beam.

Ni-filtered Cu-Kα radiation ($\lambda = 0.1542$ nm) was used, which was supplied by a mobile X-ray generator (SIEMENS Kristalloflex K710H) operated at 45 kV and 40 mA. Applying filament to film distances of 3 to 4 cm, the exposure time was 1 to 2 h. As indicated in Figure 1, on-line WAXS patterns were taken at different heights in the blowing duct and also below the spin duct. To ensure comparability between the different on-line measurements, WAXS and LLS patterns were always taken from the same filament.

Crystallinity and crystal orientation of the running filament were estimated on the basis of equatorial and azimuthal densitometer scans, respectively, taken from the on-line patterns by means of a microdensitometer (JOICE–LOEBL).

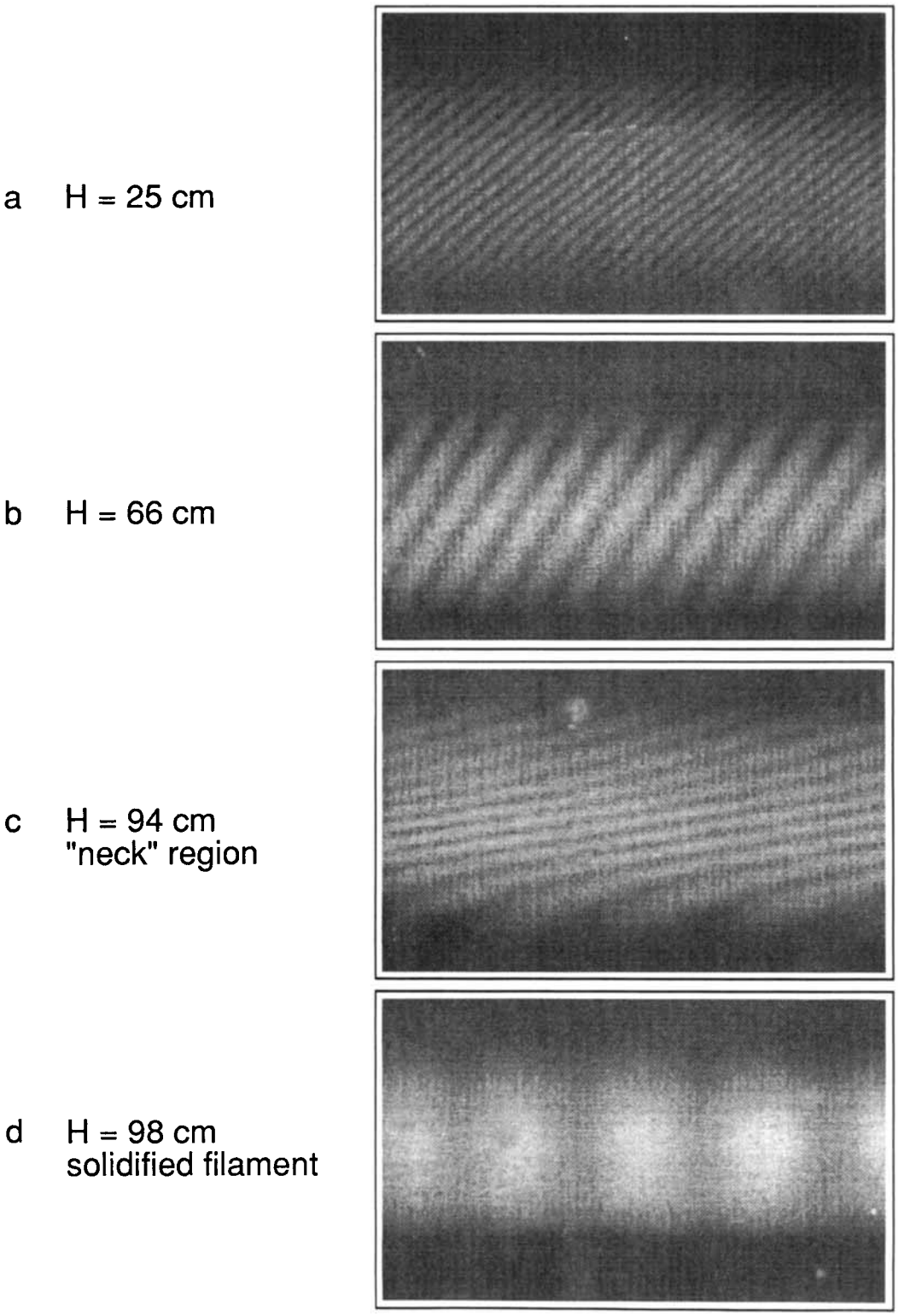

Figure 2 Typical interference patterns of PA 66 taken at different distances H from the spinneret.

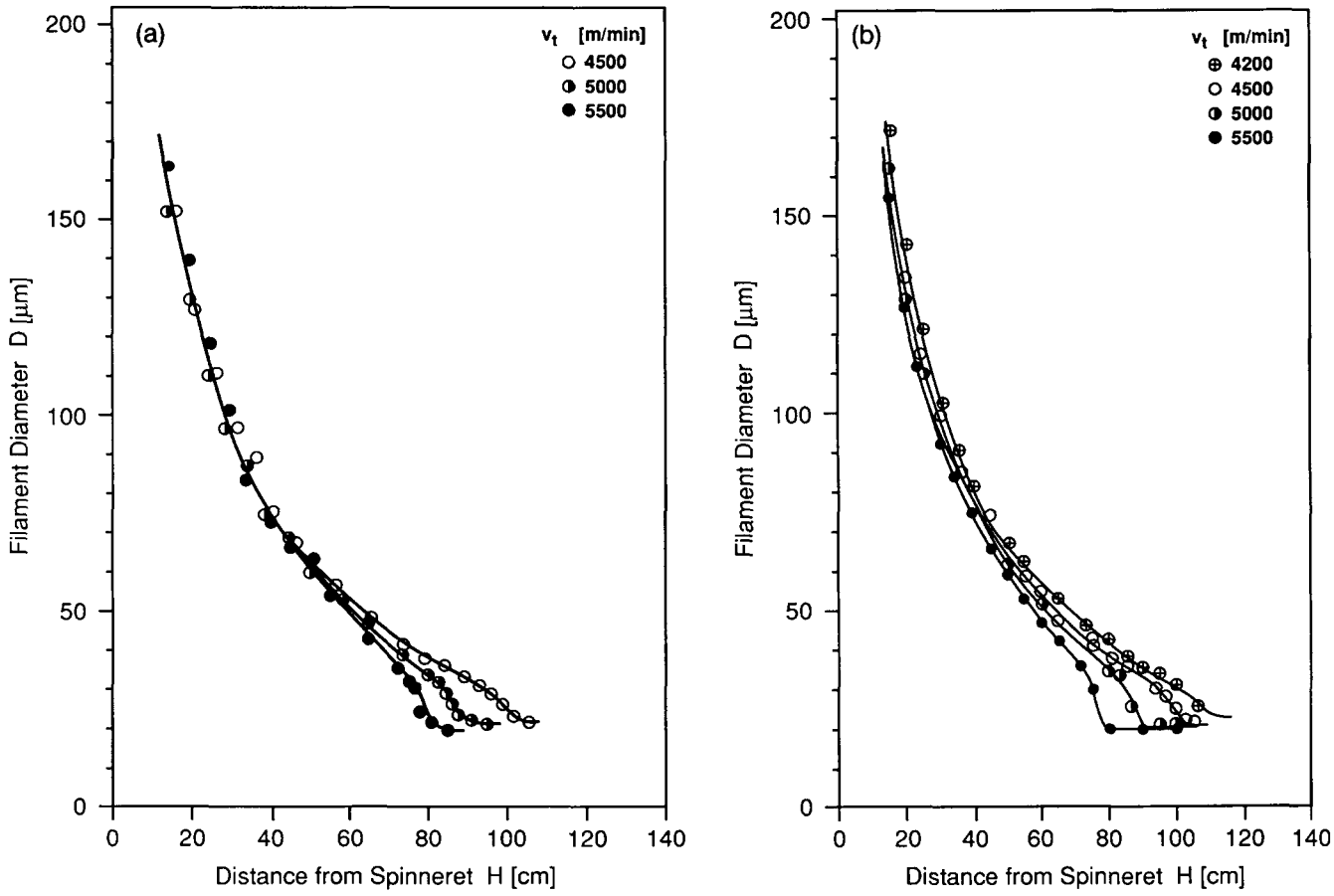

Figure 3 (a) Diameter profiles $D(H)$ of PA 66 spun at different take-up speeds v_t. Mass throughput $\dot{m}$ = 1.86 g/min/orifice. (b) Diameter profiles $D(H)$ of PA 66 spun at different take-up speeds v_t. Mass throughput $\dot{m}$ = 1.76 g/min/orifice.

RESULTS AND DISCUSSION

Diameter, Temperature, and Structure Profiles

Polyamide 66

Figures 3(a) and 3(b) show diameter profiles of PA 66 filaments spun at different take-up speeds and constant mass throughput of 1.86 and 1.76 g/min/orifice, respectively. Up to 30 cm below the spinneret, the diameter profiles are not significantly influenced by the take-up speed. For distances larger than 40 cm, the profiles split up, the draw-down being increased with increasing take-up speed. Immediately before solidification takes place, a concentrated deformation, the so-called neck-like deformation, of the filament is observed. Whereas the neck-like deformation is clearly seen for take-up speeds higher than 4200 m/min, it can be hardly perceived at 4200 m/min. With increasing take-up speed, the solidification of the filament occurs closer to the spinneret.

In Figure 4, the corresponding temperature profiles as measured for different take-up speeds are shown. The mass throughput was kept constant at 1.86 g/min/orifice. The curves clearly demonstrate that the cooling process is only slightly affected by the spinning speed, in agreement with the experimental results published in the literature.[21,22] A maximum in the temperature profile is observed at all take-up speeds. The higher the take-up speed, the higher the temperature, and consequently the smaller the distance from the spinneret at which the temperature rise occurs. The positions of the solidification points detected by LLS measurements [Fig. 3(b)] are also indicated in Figure 4 (see arrows). As can be seen, they agree with the positions of the corresponding temperature maxima.

Obviously, the temperature increase is due to the enthalpy of crystallization, which is released during the stress-induced crystallization (solidification), first observed and described for PET.[2,9,10] This conclusion is confirmed by on-line WAXS experiments,

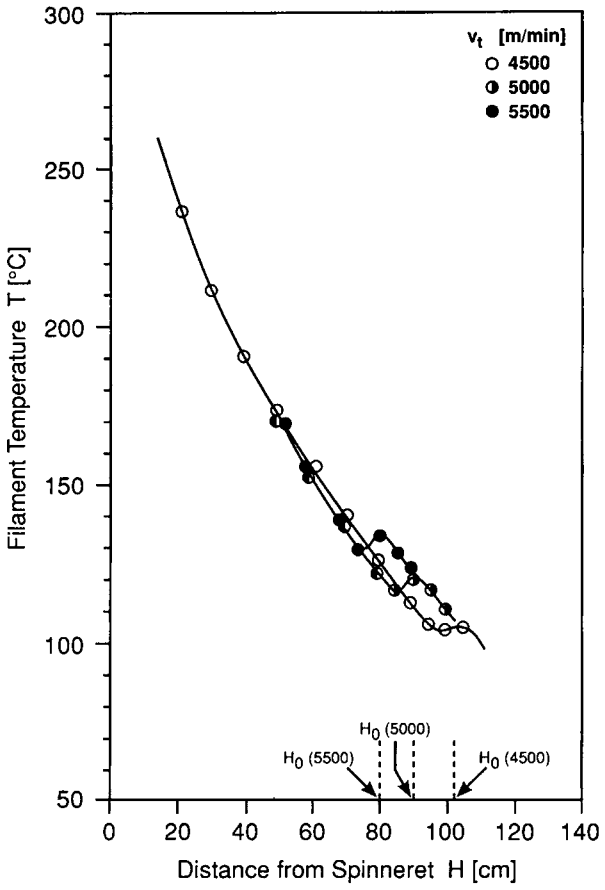

Figure 4 Temperature profiles $T(H)$ of PA 66 spun at different take-up speeds v_t. Mass throughput $\dot{m}$ = 1.86 g/min/orifice.

which show first crystalline reflections in the region of the solidification point (Fig. 7).

It should be pointed out that no conclusions with regard to the onset of crystallization, before or after the neck-like deformation, can be drawn from these data. As mentioned before, the temperature and diameter profiles were measured at two different filaments within the same thread. The LLS experiments showed that the positions of the solidification points of different filaments are generally slightly different. In addition, although the laser-light and X-ray scattering measurements were carried out at the same filament, the thread guide needed for the WAXS investigations caused the solidification point to move toward the spinneret by 1 to 3 cm.

In Figure 5, the diameter profiles of a PA 66 filament are shown, which was spun at constant take-up speed of 5500 m/min, but at different mass throughputs $\dot{m}$. With increasing mass throughput, the solidification point moves away from the spinneret. It seems as if the neck-like deformation starts at the same diameter, regardless of the mass throughput. This would mean that the deformation taking place within the neck zone increases with decreasing mass throughput.

The corresponding temperature profiles (Fig. 6) show that within the limits of experimental error (±2°C) the crystalline solidification takes place at the same temperature, regardless of the mass throughput. This suggests that the solidification temperature of a high-speed spun polymer is determined by the take-up velocity only. To test this hypothesis, the effect of other spinning parameters on the filament forming process was investigated. It was found that the solidification temperature is independent of the cooling conditions such as, for example, velocity and temperature of the cross-flow air. An increase of the orifice diameter from 250 to 350 μm (both orifices having a L/D ratio of 2) did not have any significant effect on the solidification temperature either.

In Figure 7, on-line WAXS patterns of PA 66 filaments, spun at constant take-up speed and constant mass throughput (v_t = 5500 m/min and $\dot{m}$ = 2.13 g/min/orifice, respectively), are reproduced, which were taken above and below the solidification point H_o. H_o was determined by LLS keeping the thread guide in the same position as it was held during the WAXS measurements. Above H_o [Fig. 7(a)] a diffuse intensity ring was observed, indicating that the filament was amorphous. At the solidification point [Fig. 7(b)], a pattern was obtained, in which the amorphous scattering still dominated, but in which—noticeable in the original only—first weak reflection spots of a γ-like modification appear on the equator. As can be seen in Figures 7(c) and 7(d), the intensity of the equatorial spots increased rapidly with increasing distance from H_o. This intensity increase, together with the reduction of the diffuse scattering, is an indication of an increase in crystallinity. The WAXS patterns from below the static oiler, as well as from below the spin duct, demonstrate that there are no marked changes in the scattering of the filament between a point H_c, where crystallization is completed, and the winding-up machine. The relatively high intensity of the equatorial spots in Figure 7(e) is mainly due to the greater sample volume of the thread as compared to a single filament.

In Figures 8 and 9, equatorial and azimuthal densitometer scans of the WAXS patterns of Figure 7 are shown. Both scans yield an excellent picture of

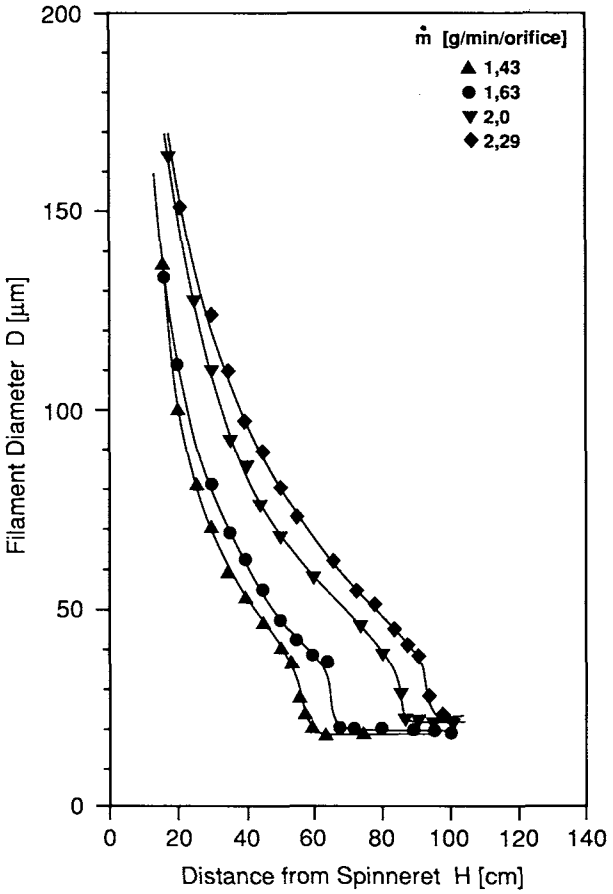

Figure 5 Diameter profiles $D(H)$ of PA 66 spun at different mass throughputs $\dot{m}$. Take-up speed v_t = 5500 m/min.

the structural changes proceeding in the running filament. The equatorial densitometer scans of Figure 8 demonstrate that high-speed spun PA 66 filaments, at least in the velocity range applied in the present investigation, crystallize in a γ-like modification. This modification is characterized by a strong reflection in the angle range $20.4° \leq 2\Theta \leq 21.4°$, the actual value in the present case being dependent on the distance ΔH from the solidification point H_o. The presence of the γ form in the spinline of high-speed spun PA 66 was also reported by Lecluse.[23]

From the equatorial scans, the height h_γ and the area F_γ, and from the azimuthal scans, the half width $\Delta\Phi_\gamma$ of the equatorial γ-like reflection were taken. The area F_γ as a rough measure of crystallinity and the reciprocal of the azimuthal half width, $\Delta\Phi_\gamma^{-1}$ $\left(= \frac{1}{\Delta\phi_\gamma}\right)$, as a measure of crystal orientation, are plotted in Figure 10 vs. the distance from the solidification point, $\Delta H = H - H_o$. Included in Figure 10 are results of a filament spun at v_t = 4500 m/min and $\dot{m}$ = 1.74 g/min/orifice and of filaments spun at v_t = 5500 m/min, but with different throughputs.

Figure 10 clearly illustrates the extremely fast oriented crystallization at or in the immediate vicinity of the solidification point. The crystallinity index F_γ rises rapidly to a plateau value, which is reached only a few centimeters below H_o [Fig. 10(a)]. In addition, an effect of v_t on the crystallization rate and crystallinity can be recognized. Filaments spun at the higher take-up speed exhibit a steeper increase as well as a higher plateau value of F_γ as compared to filaments produced with the lower take-up speed.

As follows from Figure 10(a), $\dot{m}$ has no measurable effect on crystallization rate and crystallinity. The dispersion of the F_γ curves in the steep rising region between H_o and the plateau, which is observed for these filaments, is caused by the fact that the

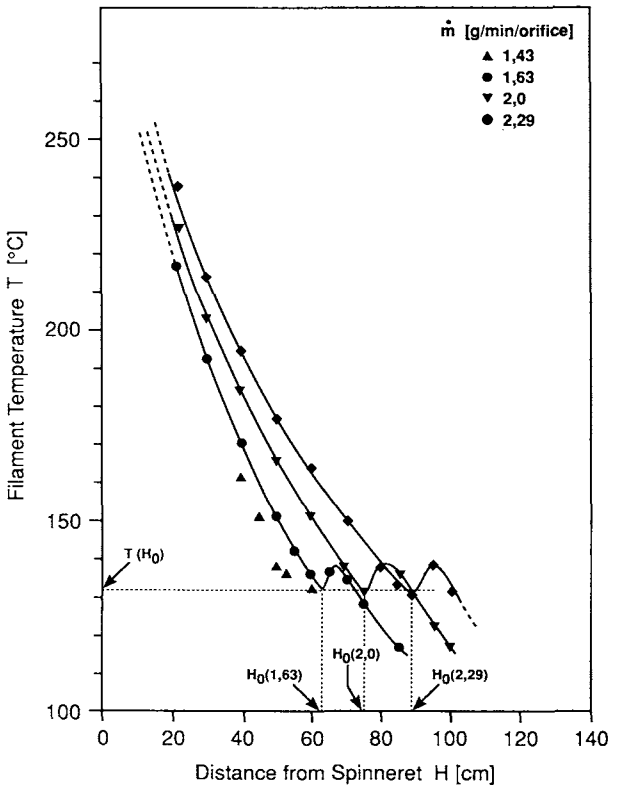

Figure 6 Temperature profiles $T(H)$ of PA 66 spun at different mass throughputs $\dot{m}$. Take-up speed v_t = 5500 m/min.

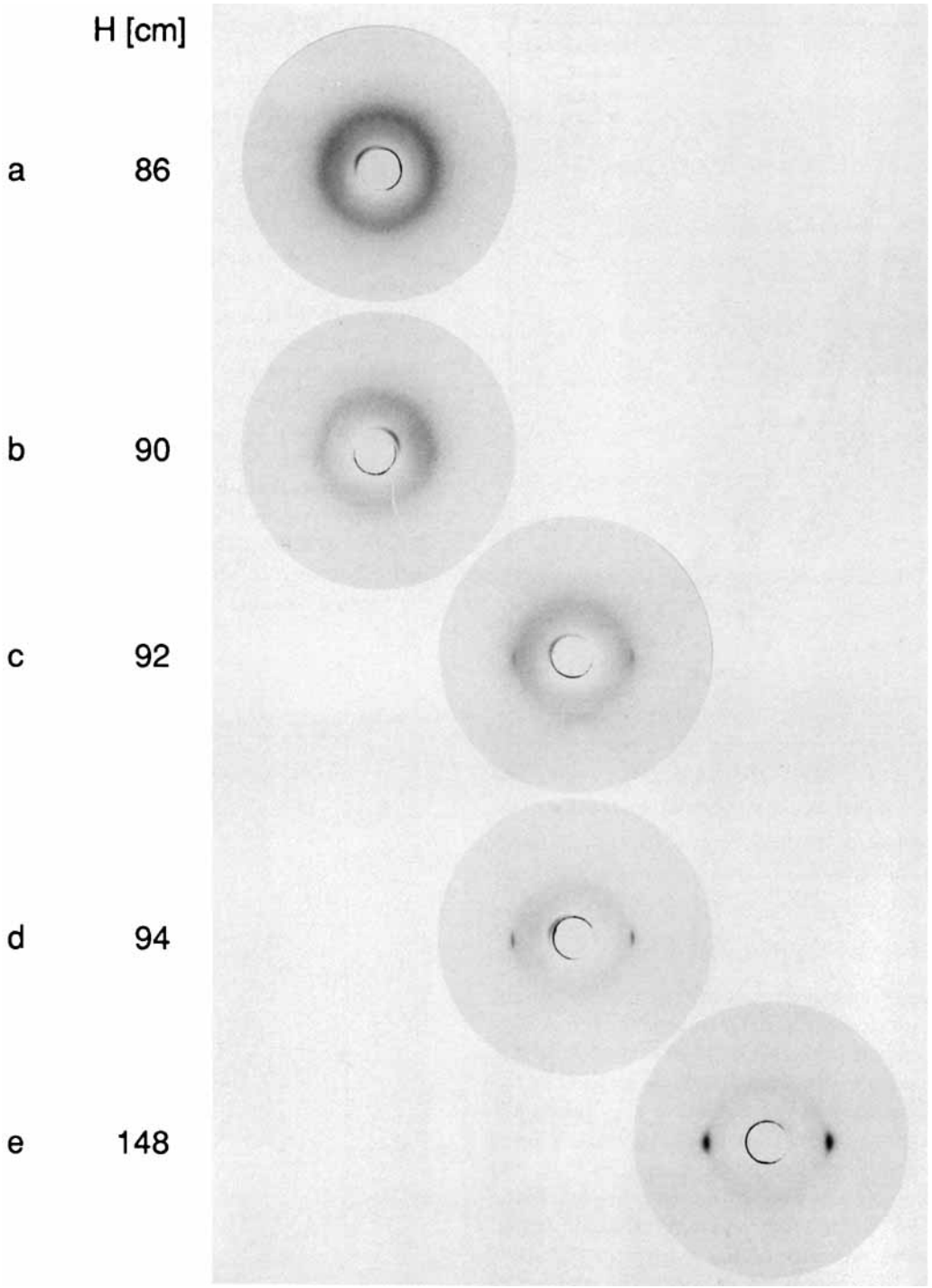

Figure 7 Typical WAXS patterns of PA 66 taken above and below the solidification point H_o. Take-up speed v_t = 5500 m/min; mass throughput $\dot{m}$ = 2.13 g/min/orifice.

position of the solidification point cannot precisely be determined (see Filament Diameter). Extrapolating the higher rising line to $F_\gamma = 0$ yields a value for H_o that is in the range of $\Delta H \approx -1.5$ cm, that is, 1 to 2 cm above the value determined by LLS.

From Figure 10(b) it follows that even the first crystals formed at the beginning of the crystallization are already highly oriented parallel to the fiber axis. This can be concluded from the relatively small azimuthal half widths $\Delta\Phi_\gamma$ of 25 to 30°. Due to the

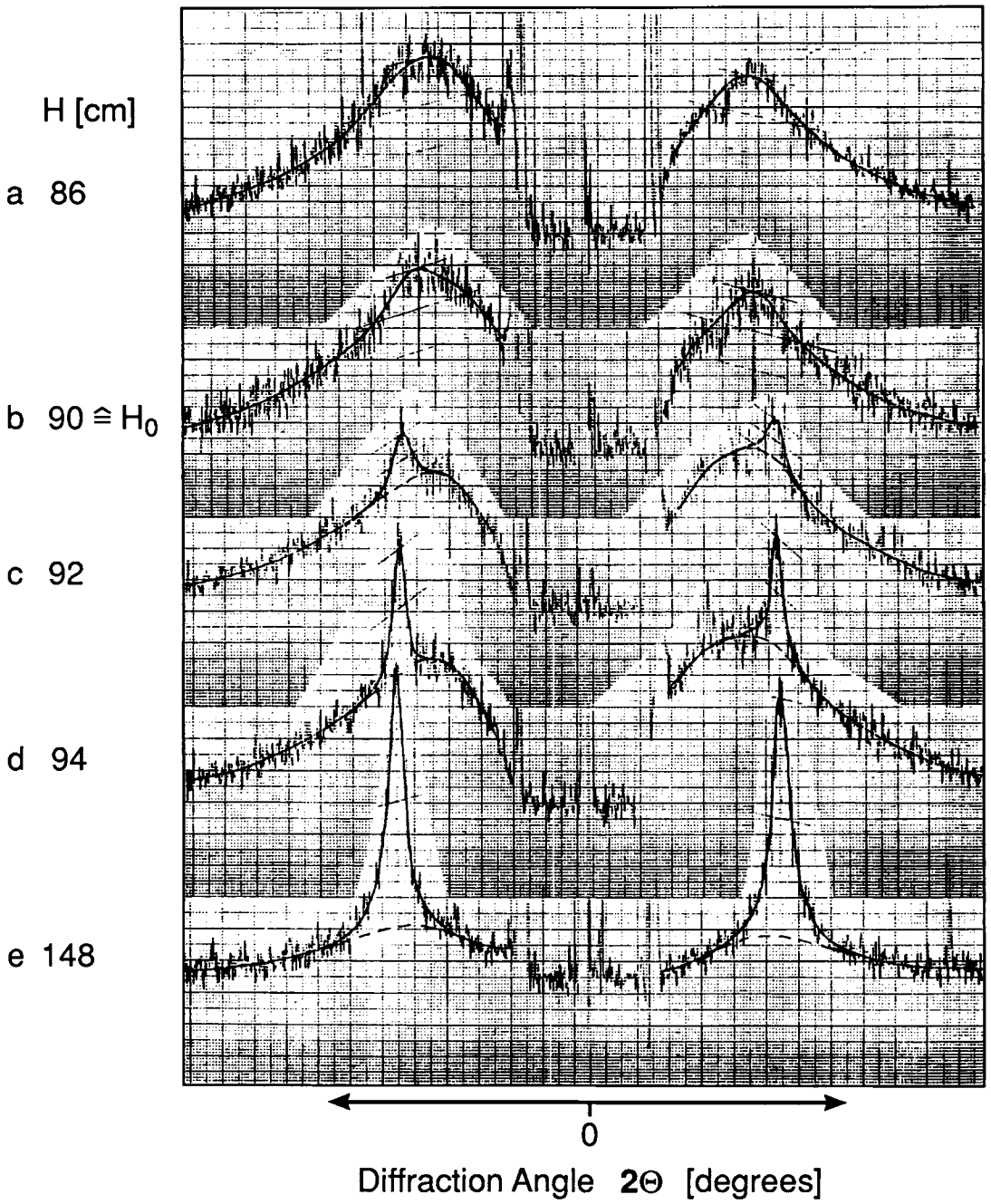

Figure 8 Equatorial densitometer scans of the on-line WAXS patterns shown in Figure 7.

weak intensity of the equatorial reflection spots in this early state of crystallization, the evaluation of $\Delta\Phi_\gamma$ is less precise as compared to that of the fully crystallized state. From the visual impression of the corresponding WAXS pattern, one can conclude that the $\Delta\Phi_\gamma$ values of these first PA 66 crystals are overestimated, that is, the true orientation should be higher than that obtained by the densitometric evaluation.

The crystal orientation also aims at a plateau, which is reached at even smaller distances ΔH from the solidification point. The effect of v_t on the pla-

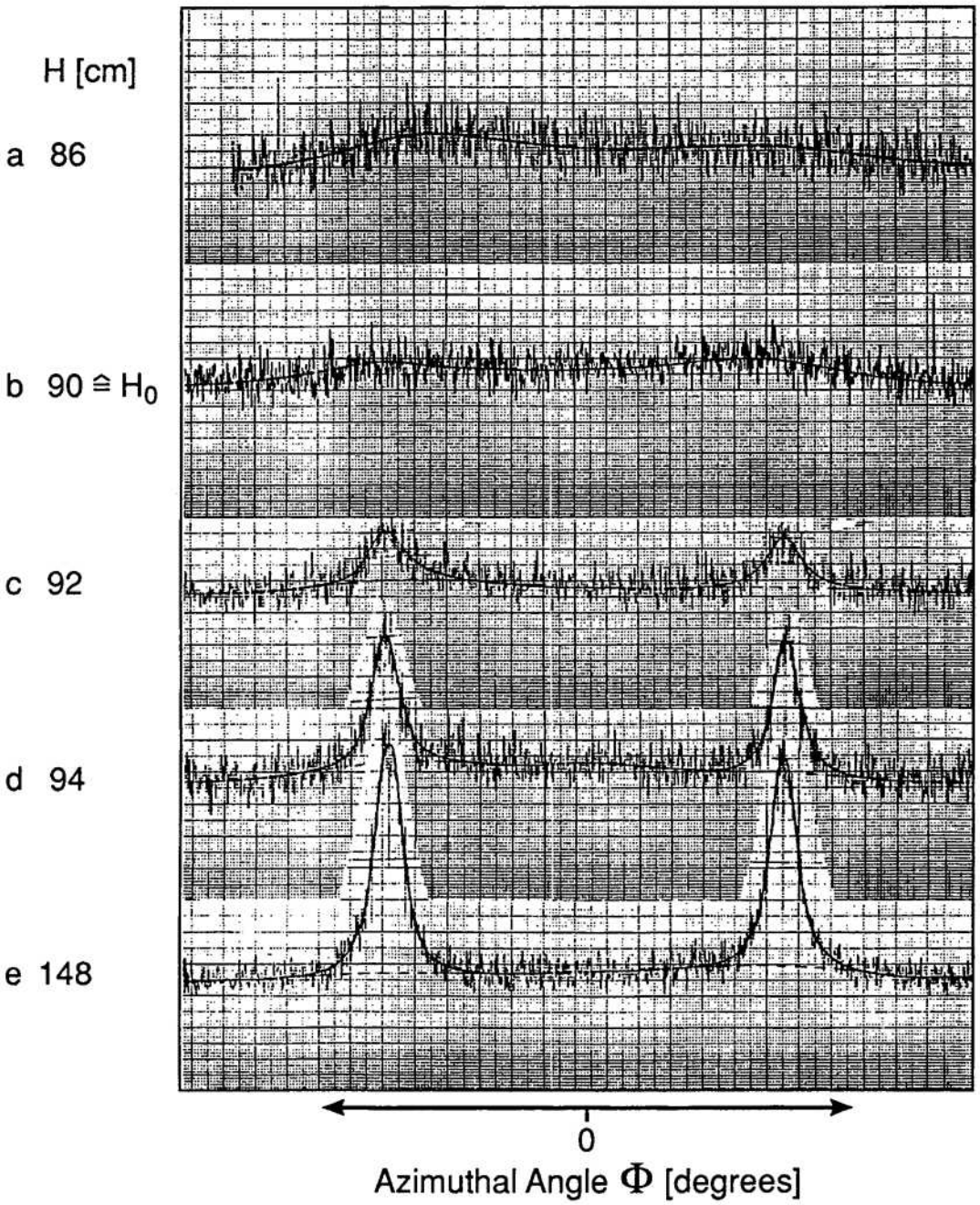

Figure 9 Azimuthal densitometer scans of the on-line WAXS patterns shown in Figure 7.

teau orientation is not as marked as for the crystallinity index. The observed differences in the plateau values of $\Delta\Phi_\gamma^{-1}$ belong to azimuthal half widths of about 17° for the lower take-up speed and of about 15° for the higher one. These values are just out of the limits of error of the evaluation, which are in the range ±0.5°. As found for the crystallinity index F_γ, the varying of $\dot{m}$ has no effect on the plateau values of the crystal orientation of the filaments.

Despite the dispersion of the F_γ values in the steep rising region, the crystallization rate can be estimated from the curves drawn in Figure 10(a). The

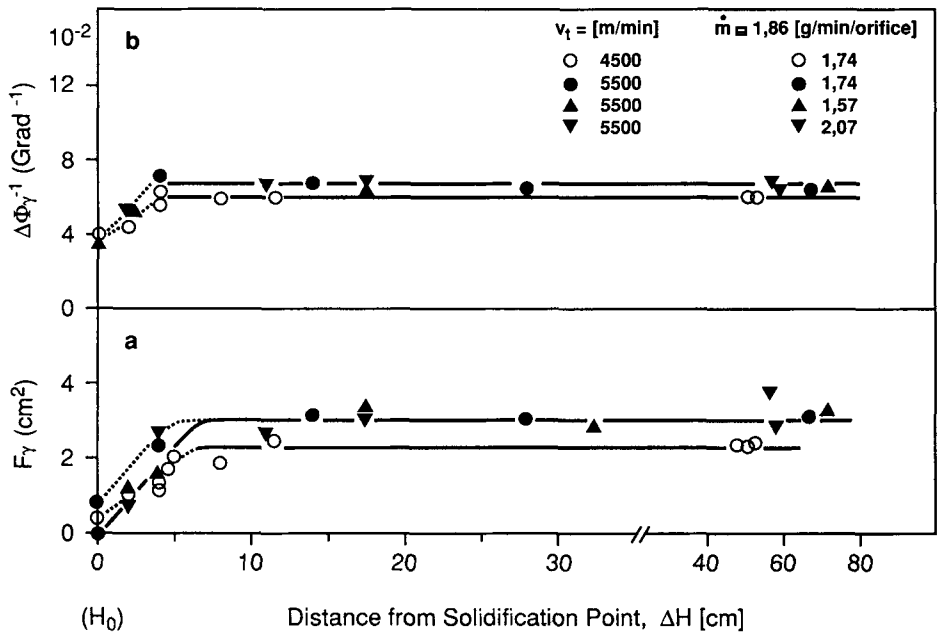

Figure 10 Crystallinity index F_γ and crystal orientation $\Delta\Phi_\gamma^{-1}$ of PA 66 filaments in dependence on the distance $\Delta H = H - H_o$ from the solidification point H_o.

half-time of crystallization, $t_{1/2}$, can be obtained by

$$t_{1/2} = \frac{\Delta H_c}{2v_t} \qquad (1)$$

where ΔH_c is the distance from the solidification point at which the plateau is reached. Taking ΔH_c to about 6 cm for v_t = 5500 m/min and to about 8 cm for v_t = 4500 cm, $t_{1/2}$ is estimated to about 0.3 ms for the higher and to about 0.5 ms for the lower take-up speed. It should be stressed that, due to the process-inherent fluctuation of H_o, the experimentally measured crystallization region ΔH_c is extended and the above estimated values represent the upper limits of $t_{1/2}$.

Polyamide 6

In Figure 11, the diameter profiles of PA 6-I are shown for different take-up speeds. For these samples, the mass throughput was increased with increasing take-up speed in order to keep the final diameter (dtex) of the filaments constant. A comparison with the diameter profiles, drawn in Figures 3(a) and 3(b), shows that the change in mass throughput reduces the effect of the spinning speed on the position of the solidification point of the filaments. PA 6 shows a neck-like deformation, which is similar to that observed for PA 66. This result already indicates that PA 6, like PA 66 and PET, solidifies by a stress- (orientation-) induced crystallization process.

As follows from the temperature profiles of Figure 12, the cooling rate decreases with increasing mass throughput. Similar to PA 66, the solidification temperature increases with increasing take-up speed. Because of the reduced cooling rate at higher mass throughput, the increase of the solidification temperature causes only small differences in the position of the solidification point H_o.

Although the solidification temperatures of PA 6-I are similar to those of PA 66, there is a major difference in the temperature curves of both polyamides. Whereas the temperature profiles of PA 66 show a pronounced maximum, a more plateau-like behavior is observed for PA 6-I. This suggests that the crystallization rate is higher for PA 66 than for PA 6. As is discussed later, this conclusion is confirmed by the on-line WAXS data.

In Figure 13, the diameter profiles of PA 6-I and PA 6-II, spun at a take-up speed of 4500 m/min and at a mass throughput of 1.76 g/min/orifice, are compared. The spinning temperatures were 278°C and 288°C for PA 6-I and PA 6-II, respectively. The draw-down of PA 6-II, the polymer of the higher

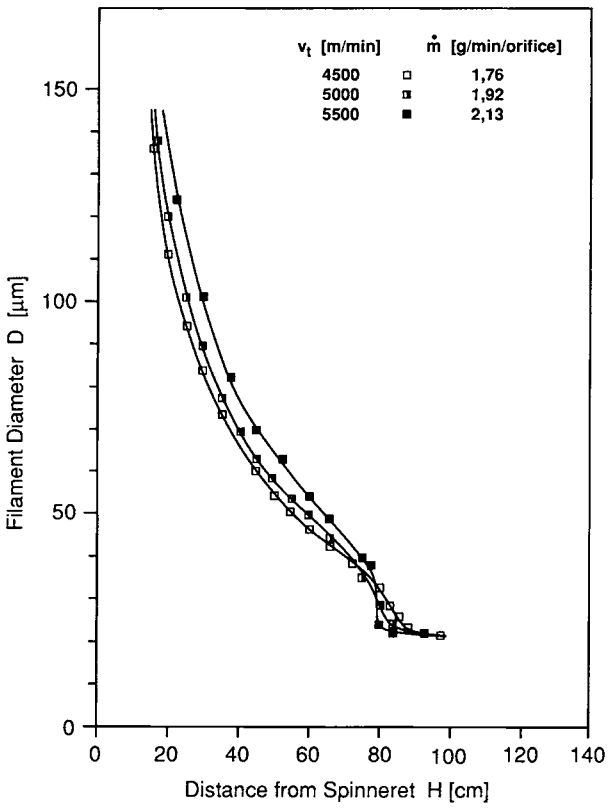

Figure 11 Diameter profiles $D(H)$ of PA 6-I of constant final diameter.

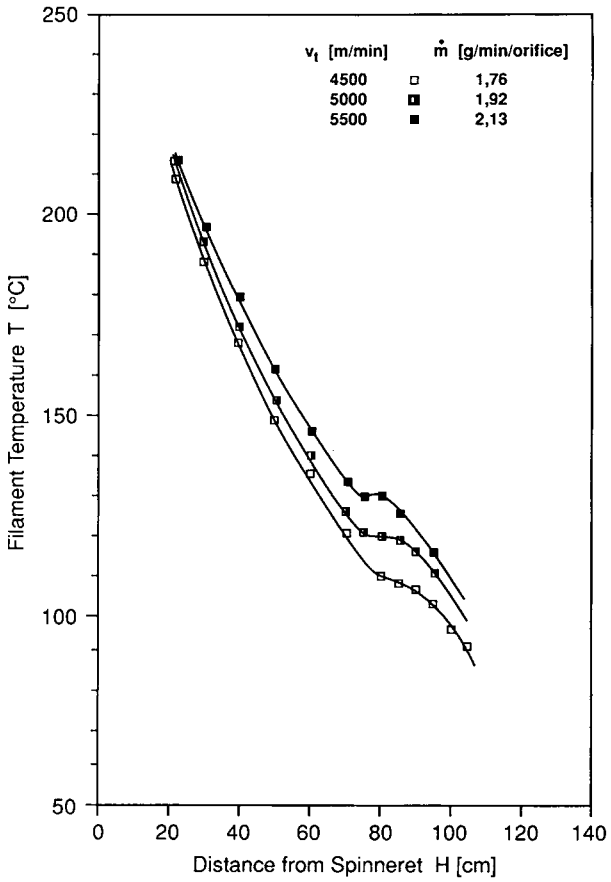

Figure 12 Temperature profiles $T(H)$ of PA 6-I of constant final diameter.

molecular mass, occurs significantly faster than that of PA 6-I of the lower M_n. This results in a solidification point of PA 6-II, which is nearly 20 cm closer to the spinneret than that of PA 6-I. As follows from the temperature profiles shown in Figure 14, the solidification temperature of PA 6-II is about 16 degrees higher than that of PA 6-I. The solidification temperature of both PA 6 filaments was found to be independent of the mass throughput and the processing temperature. Different cooling conditions and different orifice diameters were not investigated for PA 6.

From the present results, it can be concluded that within the range of take-up speeds considered, the solidification temperatures of PA 66 and PA 6 are exclusively determined by the take-up speed v_t and are independent of all other spinning parameters.

The crystallization behavior of PA 6 was also studied by on-line WAXS measurements. In Figure 15, WAXS patterns of a PA 6-I filament are reproduced, which was spun at v_t = 5500 m/min and $\dot{m}$ = 2.19 g/min/orifice. As observed for PA 66, crystallization of the running PA 6 filament starts at or in the immediate vicinity of the solidification point H_o [Fig. 15(b)]. With increasing distance from H_o, the typical scattering pattern of the uniaxially oriented γ modification of PA 6 occurs, which is characterized by both a strong equatorial and a strong meridional reflection spot.

From the WAXS patterns, no indication for the presence of α crystals could be obtained. So, the on-line crystallization of high-speed spun PA 6 filaments seems to produce not the usual γ-α polymorphism, but only the pure γ form. The γ crystals formed along the spinline were relatively stable. Therefore, they were forming the main part of the crystalline phase also after winding up the filaments. This is confirmed by the results of Heuvel and Huisman,[24] obtained with as-spun PA 6 yarns after conditioning them at 20°C and 60% relative humidity,

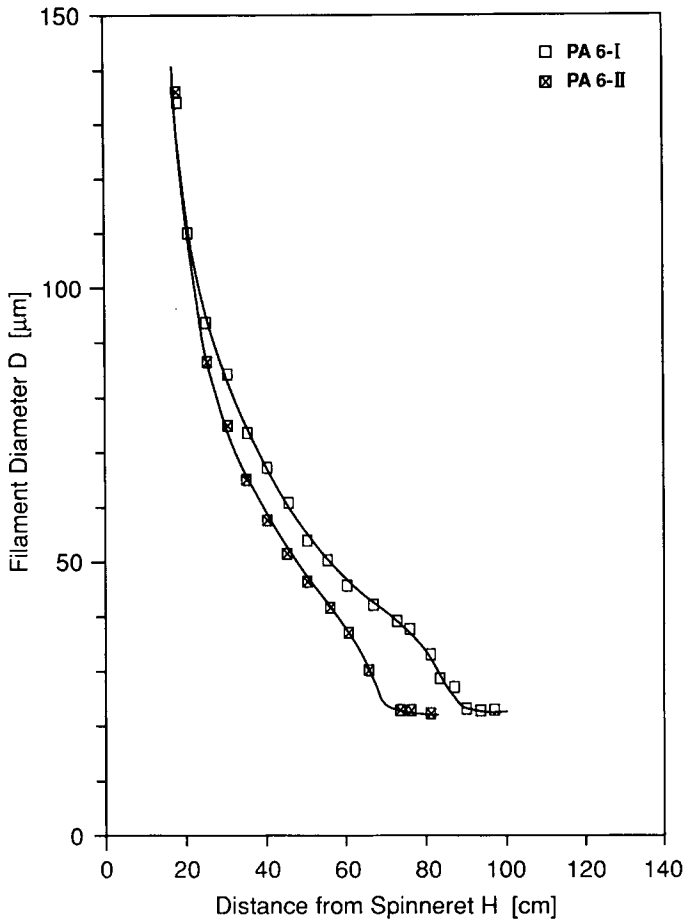

Figure 13 Diameter profiles $D(H)$ of PA 6 filaments of different molecular masses M_n. Take-up speed v_t = 4500 m/min; mass throughput $\dot{m}$ = 1.76 g/min/orifice.

and by the work of Koyama, Suryadevara, and Spruiell.[25]

The equatorial as well as the azimuthal intensity distributions of the equatorial spot, as measured by microdensitometry, were again evaluated with respect to crystallinity and crystal orientation. The result of these evaluations is given in Figure 16, completed by the data obtained for a filament series spun at 4500 m/min. The crystallinity index F_γ and the crystal orientation $\Delta\Phi_\gamma^{-1}$ of PA 6-I show a similar increase with the distance ΔH from the solidification point H_o as was found for PA 66. Again the effect of the take-up speed can clearly be recognized.

There are two characteristic differences, however, when comparing the WAXS results obtained for PA 66 and PA 6 (Figures 10 and 16). First, at the take-up speeds applied in this investigation, PA 66 filaments always crystallized more rapidly than PA 6 filaments did. Second, the plateau orientation of PA 6 was higher than that of PA 66. In addition, the effect of v_t on the crystal orientation was more pronounced for PA 6 as compared to PA 66, where only a modest increase with v_t was observed [Fig. 10(b)].

These differences can be recognized in Figure 17, in which the parameters F_γ and $\Delta\Phi_\gamma^{-1}$ are compared for PA 66 and PA 6-I filaments both spun at v_t = 5500 m/min. Estimating the crystallization rate in the same manner as described for PA 66 yields values for the crystallization half-time $t_{1/2}$, which are higher for PA 6-I by a factor of about 2 than those obtained for PA 66 (Table II). As emphasized above, these data represent the upper limits of the crystallization half-times, that is, the true crystallization rates of high-speed spun polyamides are even higher.

As follows from Figures 7 and 15, the first crystallites formed at or just below the solidification point H_o already show a marked orientation parallel

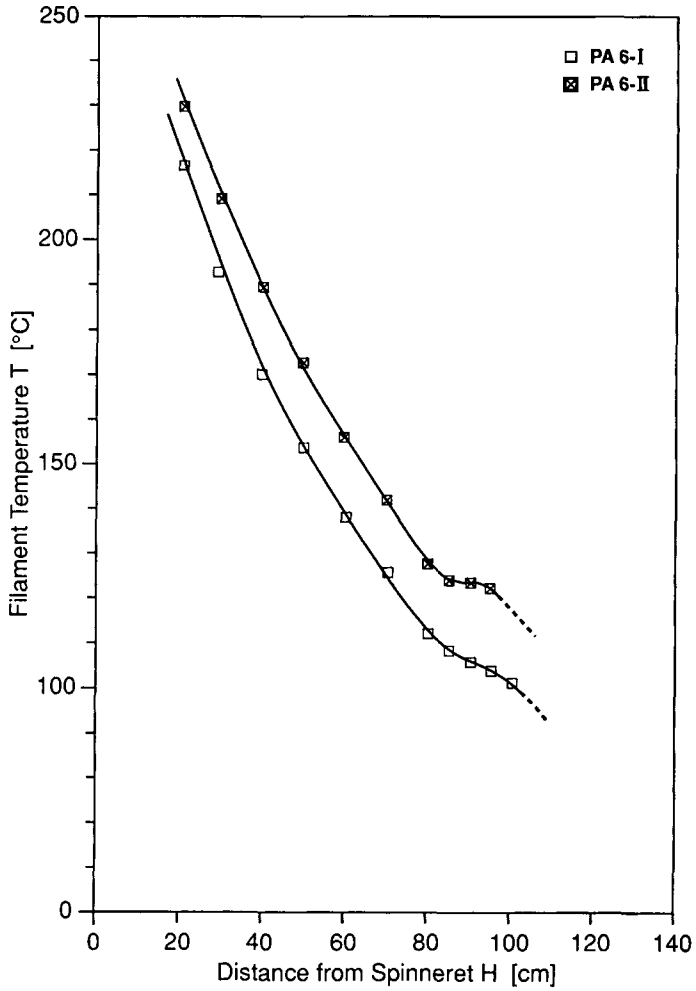

Figure 14 Temperature profiles $T(H)$ of PA 6 filaments of different molecular masses M_n. Take-up speed v_t = 4500 m/min; mass throughput $\dot{m}$ = 1.76 g/min/orifice.

to the fiber axis, the degree of orientation being increased within the crystallization region ΔH_c. It is likely that this fast oriented crystallization originates from nuclei of high molecular orientation induced in at least parts of the running, still molten filament immediately before crystallization.

Due to the theoretical considerations of Ziabicki and Jarecki,[26,27] the nucleation rate in an oriented polymer melt is strongly dependent on the inclination Φ of the molecules with respect to the fiber axis. For segments that are fully parallel to the fiber axis ($\Phi = 0$), the nucleation and the crystallization rate are higher by many orders of magnitude than for segments being significantly inclined or even perpendicular to the fiber axis.

Besides this theoretical work, the influence of molecular orientation on the crystallization rate and crystallinity has been experimentally studied by several authors[28-30] who investigated the relatively slowly crystallizing PET. As shown in Ref. 28, the crystallization half time is reduced from about 10 min for isotropic bulk PET to 20 s for a moderately oriented PET fiber and to < 10 ms for a highly oriented one. So, highly oriented amorphous PET is characterized by crystallization rates that are 4 to 5 orders of magnitude higher than that of unoriented amorphous PET.

For the present high-speed spun polyamide filaments, no direct experimental data concerning the degree of molecular orientation, such as birefringence or orientation factor, have been measured. However, there is indirect evidence for a high ori-

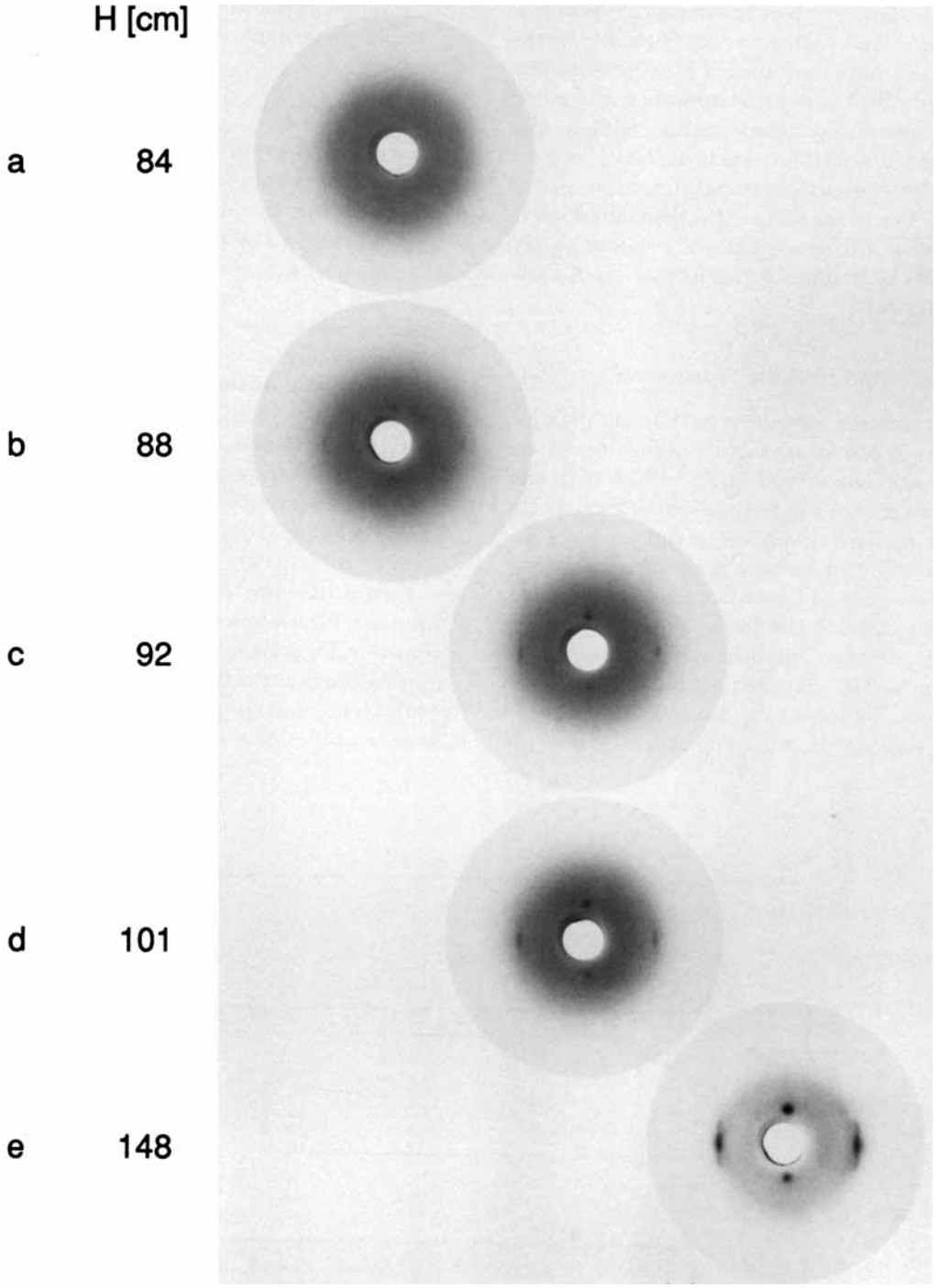

Figure 15 Typical WAXS patterns of PA 6-I taken above and below the solidification point H_o. Take-up speed v_t = 5500 m/min; mass throughput $\dot{m}$ = 2.13 g/min/orifice.

entation immediately before the onset of crystalline solidification of the filaments. As is shown in the Tensile Stress and Instantaneous Elongational Viscosity section, the filament tension and, according to the stress optical law,[31] the frequency of molecular segments, which are only weakly inclined or even parallel to the fiber axis, strongly increase in the neck region. As a consequence, the concentration of oriented nuclei will be significantly higher at the end of the neck, leading to the formation of well-oriented γ crystals.

Investigation of the Necking Process

Due to the random movement of the solidification point, only an approximate picture of the draw-down within the neck region was given by the diameter profiles thus far (see the evaluation method of the light scattering data described in the section Filament Diameter). Contrary to point-like measuring devices, for example, a Laser Doppler anemometer, the line-like shape of the laser beam used in the present experiments enabled the simultaneous measurement of the diameter profile over a length of about 4 cm. By means of this special feature of the optical equipment, we were able to study the neck-like deformation in greater detail, despite the random movement of the solidification point.

Diameter Profile

Figure 18 shows three interference patterns representing "snap shots" of a PA 66 filament taken at the beginning, in the center, and at the end of the necking region (take-up speed 5500 m/min). The changes of the filament diameter were immediately reflected by the changes of the inclination of the interference stripes. The interference stripes can approximately be considered as envelopes of the diameter profile. At the beginning of the neck-like deformation, the inclination, and therefore the deformation rate, increases, goes through a maximum in the center, and decreases again at the end of the neck region just before the filament solidifies. As can be seen from the third interference pattern, the solidification occurs abruptly.

Figure 19 shows the diameter profile determined from six interference patterns, three of which are shown in Figure 18. The position chosen for the solidification point is also indicated in Figure 18. The evaluation of each scattering picture gives the diameter profile of a limited part of the neck region

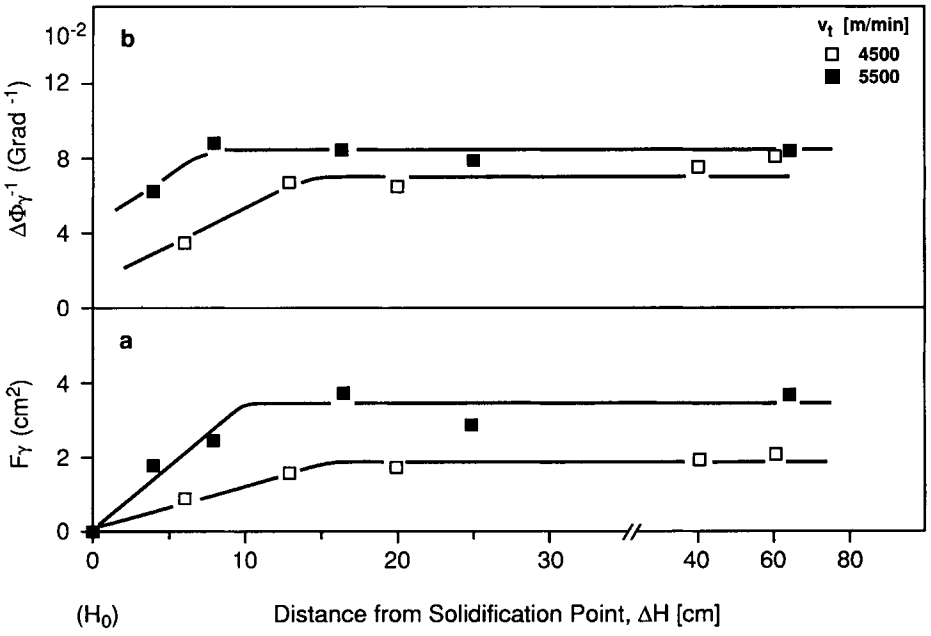

Figure 16 Crystallinity index F_γ and crystal orientation $\Delta\Phi_\gamma^{-1}$ of PA 6-I filaments in dependence on the distance $\Delta H = H - H_o$ from the solidification point H_o. Mass throughput $\dot{m}$ = 2.19 g/min/orifice.

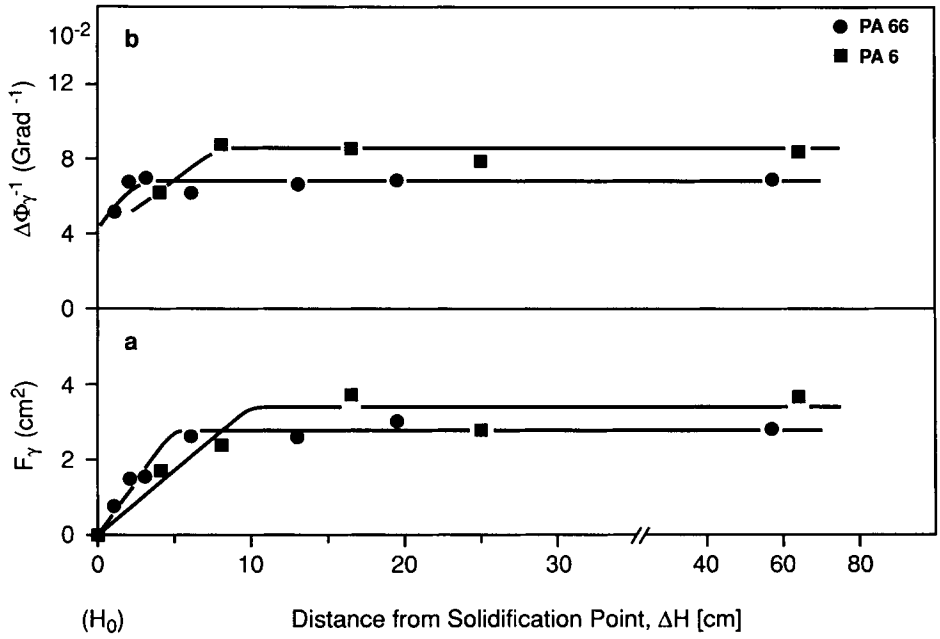

Figure 17 Crystallinity index F_γ and crystal orientation $\Delta\Phi_\gamma^{-1}$ of PA 66 and PA 6-I filaments in dependence on the distance $\Delta H = H - H_o$ from the solidification point H_o. Take-up speed v_t = 5500 m/min; mass throughput $\dot{m}$ = 2.19 g/min/orifice.

only. By shifting these parts along the H-axes, they were fitted together to yield the diameter profile shown in Figure 19.

As can be seen, the neck-like deformation takes place over a length ΔH_n of about 6 to 7 cm at a take-up speed of 5500 m/min. At a take-up speed of 4500 m/min this length increases to about 10 to 12 cm. These data clearly demonstrate that the neck-like deformation in high-speed spinning should not be confused with the necking observed in the cold-drawing of fibers spun at conventional speeds (v_t < 1000 m/min). In this case, the reduction ΔD of the filament diameter takes place over much shorter distances $\Delta H_n \sim \Delta D$.

Table II Crystallization Half-Times $t_{1/2}$ of PA 66 and PA 6 Filaments as Estimated from the Crystallization Profiles F_γ (ΔH)

	$t_{1/2}$ (ms)	
v_t (m/min)	PA 66	PA 6-I
4500	0.5	1.0
5500	0.3	0.6

In Figure 20, the axial velocity v_a within the neck is plotted vs. the "running time" Δt. v_a and Δt were calculated from the diameter profile shown in Figure 19 according to the equations

$$v_a = \frac{4\dot{m}}{\pi\rho_f D^2} \tag{2}$$

$$\Delta t = \int_{H_o-7\text{ cm}}^{H} \frac{dx}{v_a(x)} \tag{3}$$

assuming a constant filament density ρ_f = 1.10 g/cm^3. From the first derivative of this curve, a maximum acceleration of 3000 g, where g is the acceleration due to gravity, is obtained.

Simultaneous Temperature and Diameter Measurements

To understand the molecular processes causing the neck-like deformation, it is important to know where along the neck zone the crystalline solidification occurs. As the onset of crystallization results in a temperature rise of the filament, this question can be investigated by measuring simultaneously the temperature and diameter profile of the same filament.

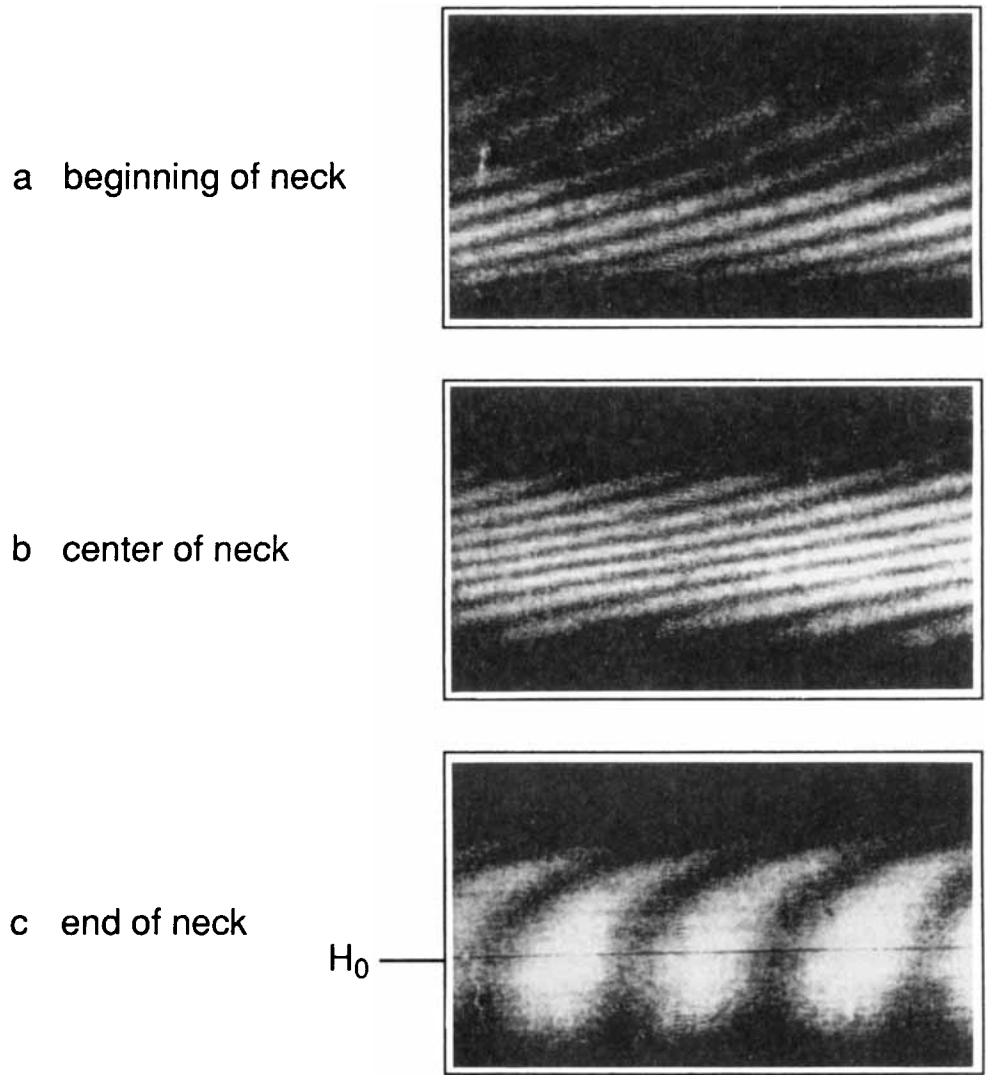

Figure 18 Interference patterns of PA 66 from the neck region representing "snap shots" taken (a) at the beginning, (b) in the center, and (c) at the end of the neck region. Take-up speed v_t = 5500 min; mass throughput $\dot{m}$ = 1.86 g/min/orifice.

Correspondingly, experiments were carried out by focusing the line-like shape of the laser beam on that part of the filament that was running in front of the heated reference plate used for the thermographic temperature measurements. The centers of the plate and the laser beam were adjusted to the same height. To make sure that the temperature and diameter readings were taken at the same point, the filament temperature was determined at the center of the reference plate, and the filament diameter was evaluated using the distances between the interference stripes from the center of the scattering pattern.

The diameter and temperature profiles evaluated in this way for a PA 66 filament are shown in Figures 21(a) and 21(b) for take-up speeds of 4500 and 5000 m/min, respectively, and $\dot{m}$ = 1.86 g/min/orifice. As can be seen from both drawings, the temperature starts to increase at the end of the neck-like deformation. The broken vertical lines indicate the region where a definite determination of the filament diameter and the filament temperature were not possible. In this region, the interference patterns fluctuated between fully solidified (vertical interference stripes) and not yet solidified (highly inclined interference stripes), as the solidification point moved up and down.

A similar behavior was observed for the ther-

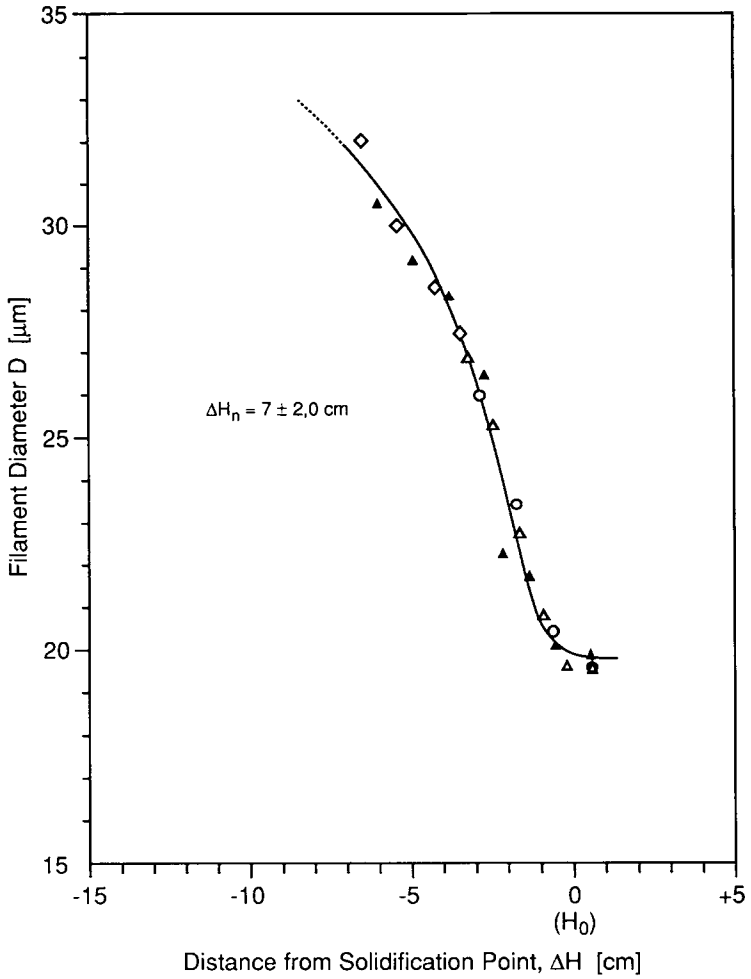

Figure 19 Diameter profile $D(H)$ of PA 66 measured in the neck region ΔH_n. Take-up speed v_t = 5500 m/min; mass throughput $\dot{m}$ = 1.86 g/min/orifice.

mographic measurements. The contrast between filament and reference plate was compensated in the center of the reference plate. As long as the filament temperature decreased along the spin line, the filament appeared light vs. the reference plate in the upper half and dark in the lower half of the reference plate. In the region where the temperature increased with increasing distance from the spinneret, the filament appeared dark vs. the reference plate in the upper half and light in the lower half of the reference plate. Due to the movement of the solidification point, the position at which the transition of the infrared picture occurred moved randomly up and down by about ±2 cm. The statistical nature of this movement made it impossible to assign unambiguously the optical and thermographic pictures to each other in a transition region of about 4 cm, which is indicated in Figures 21(a) and 21(b) by broken vertical lines.

In the transition region, the minimum and maximum filament temperatures, that is, the temperatures before and after the onset of crystallization, were estimated to be 100°C and 103°C at v_t = 4500 m/min and 111°C and 116°C at v_t = 5000 m/min. For the temperature profiles shown in Figures 21(a) and 21(b), the mean values of these temperatures were used at distances H = 105 cm (4500 m/min) and 89 cm (5000 m/min) from the spinneret. At both spinning speeds, the temperature transition from the coldest to the warmest point of the filament occurred within a distance smaller than 4 cm, indicating that the crystallization takes place rapidly (see Figs 10 and 17).

These results demonstrate that crystallization

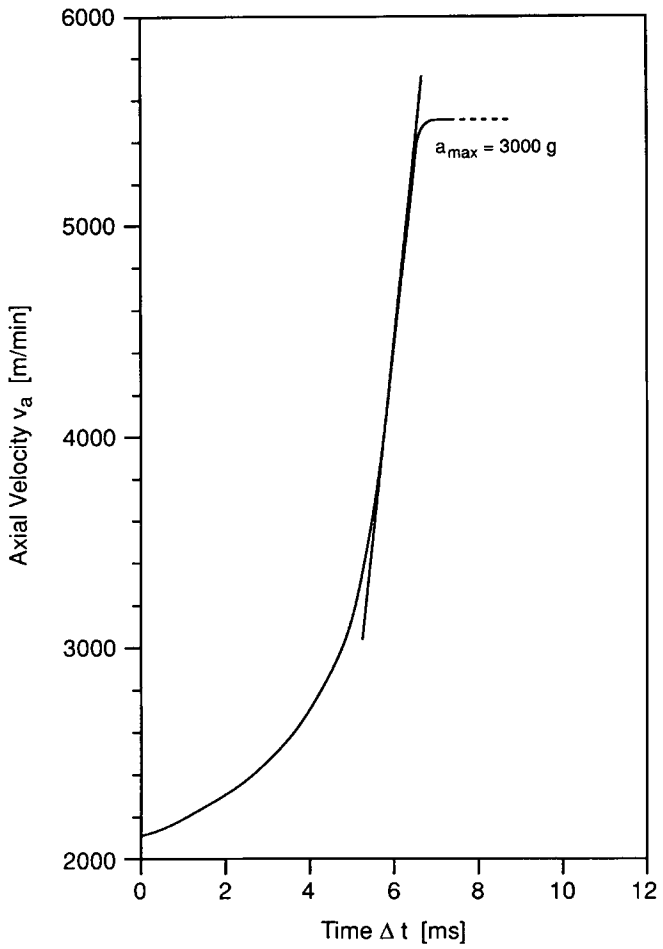

Figure 20 Time dependence of the axial velocity v_a of PA 66 in the neck region ΔH_n. Take-up speed v_t = 5500 m/min; mass throughput $\dot{m}$ = 1.86 g/min/orifice.

takes place at the end of the neck-like deformation process, less than 2.5 cm above the solidification point H'_o. Due to the limited measurement accuracy and the difficulty of defining a "solidification point" clearly, a more precise determination of the onset of crystallization was not possible. Despite this uncertainty, it follows from Figure 21(a) (v_t = 4500 m/min) that most of the concentrated deformation within the neck zone has already taken place before crystallization occurs. The situation is not so clear for a take-up speed of 5000 m/min. In this case, due to the smaller range of the neck zone, one cannot exclude from the present measurements that a considerable amount of the concentrated draw-down—as much as 40%—occurs after the onset of crystallization [Fig. 21(b)].

Based on the fact that crystallization takes place at the end of, or even after, the neck-like deformation, it can be concluded that the formation of a neck is not primarily caused by the onset of the crystalline solidification of the filament. This means that the neck-like deformation cannot be explained, for example, by a reduction of the elongational viscosity due to the heat of crystallization or by a spontaneous elongation upon crystallization.[32] This does not mean, however, that the formation of the neck is not related to crystallization at all.

Oriented Crystallization in the Neck Region

In order to get additional information about the development of the structure in the neck region, the diameter and temperature measurements were complemented by WAXS experiments carried out at the same filament. The result of these combined investigations of a PA 66 filament, spun at v_t = 5000

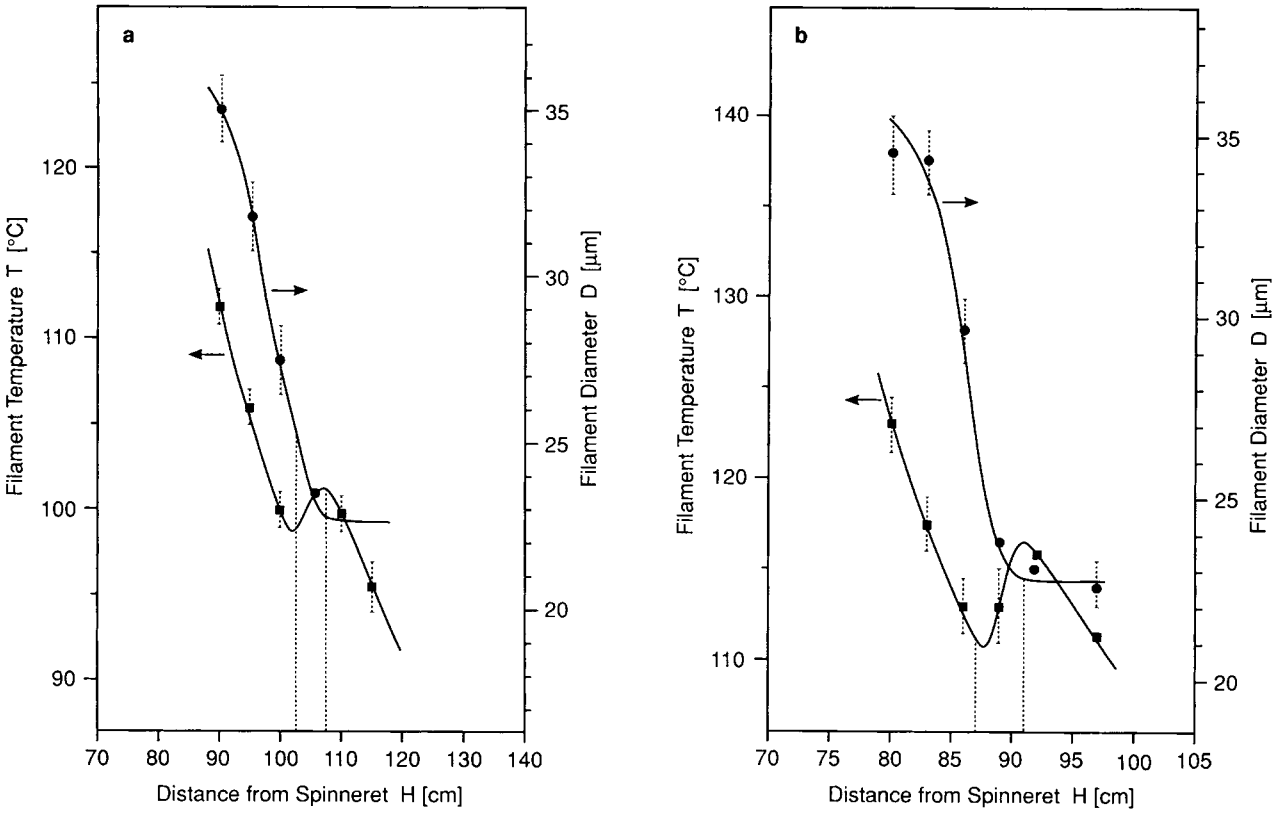

Figure 21 (a) Diameter profile $D(H)$ and temperature profile $T(H)$ of PA 66 simultaneously measured in the neck region. Take-up speed v_t = 4500 m/min; mass throughput $\dot{m}$ = 1.86 g/min/orifice. (b) Diameter profile $D(H)$ and temperature profile $T(H)$ of PA 66 simultaneously measured in the neck region. Take-up speed v_t = 5000 m/min; mass throughput $\dot{m}$ = 1.86 g/min/orifice.

m/min and $\dot{m}$ = 1.91 g/min/orifice, is reproduced in Figure 22. Despite the experimental error of ±2 cm, which has to be considered for the position of H_o, the WAXS patterns confirm the evidence given above. The first crystalline reflection spots occur at the end of the neck-like reduction of the filament diameter whereas at the beginning as well as in the center of the neck only the diffuse scattering ring of the amorphous filament can be observed in the WAXS patterns.

DEVELOPMENT OF THE MOLECULAR STRUCTURE ALONG THE SPINLINE

Tensile Stress and Instantaneous Elongational Viscosity

Based on the diameter data, the profiles of the elongation rate $\dot{\epsilon}(H)$ and tensile stress $\sigma(H)$ were calculated according to the equations[26]:

$$\dot{\epsilon}(H) = -\frac{8\dot{m}}{\pi\rho D^3}\frac{dD}{dH} \tag{4}$$

$$\sigma(H) = \frac{4}{\pi D^2}\left(-F_G(H) + F_D(H) + F_I(H) + F_S(H) + F_o\right) \tag{5}$$

where $\dot{m}$ is the mass throughput per orifice and ρ is the polymer density, which was approximated by a constant value of 1.10 g/cm^3. F_G is the gravitational force, F_D the air drag force, F_I the inertial force, and F_S the surface tension force given in Ref. 26. The dependence of these forces on H was obtained from the measured diameter profiles. F_o is a constant force, which was determined from the relation:

$$F_o = \frac{4}{\pi D(0)^2}\dot{\epsilon}(0)\cdot\mu(0) \tag{6}$$

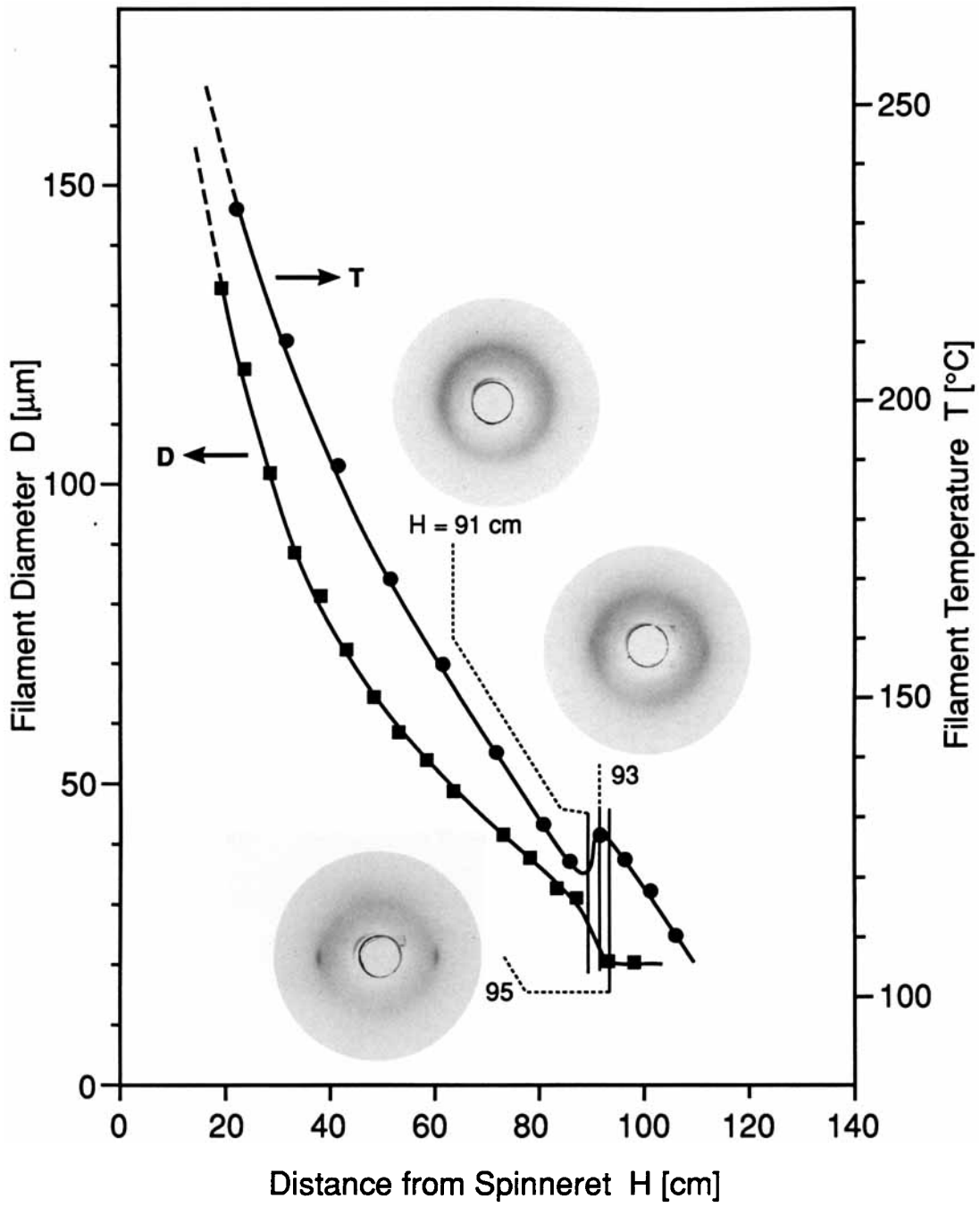

Figure 22 Diameter profile $D(H)$, temperature profile $T(H)$, and WAXS patterns of PA 66 in the neck region. Take-up speed v_t = 5000 m/min; mass throughput $\dot{m}$ = 1.93 g/min/orifice.

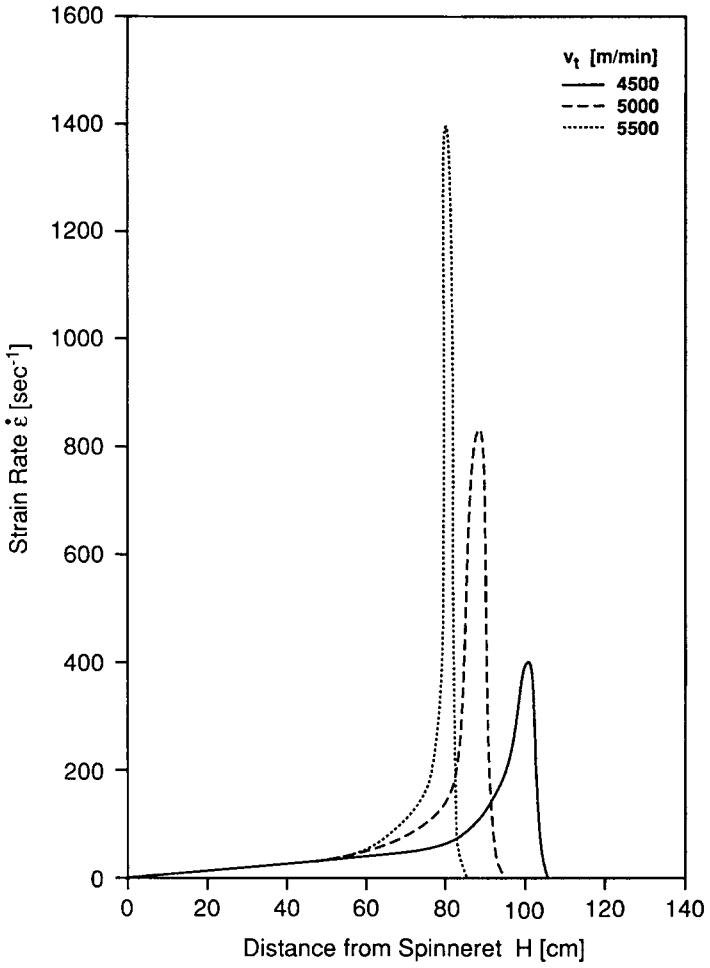

Figure 23 Strain rate profiles $\dot{\epsilon}(H)$ of PA 66 filaments spun at different take-up speeds v_t. Mass throughput $\dot{m}$ = 1.86 g/min/orifice.

The filament diameter $D(0)$ and the elongation rate $\dot{\epsilon}(0)$ at $H = 0$ were obtained from measurements of the diameter profile directly below the spinneret surface.

The elongational viscosity $\mu(0)$ was determined from the shear viscosity according to the Trouton relation:

$$\mu = 3\eta_o \tag{7}$$

where η_o is the Newtonian shear viscosity. A value of η_o = 60 Pa · s[33] was used for PA 66 at the spinning temperature of 297°C. From the tensile stress and the elongation rate, the instantaneous elongational viscosity was determined as:

$$\mu_i(H) = \frac{\sigma(H)}{\dot{\epsilon}(H)} \tag{8}$$

where μ_i describes the experimentally observed elongational behavior. Only if the deformation process takes place in a quasi-steady state, that is, if transient viscoelastic effects can be neglected, it will be identical with the steady-state elongational viscosity $\mu(H)$.

In Figure 23, the profile of the elongation rate $\dot{\epsilon}(H)$ is shown for three different take-up speeds (v_t = 4500, 5000, and 5500 m/min) at a constant mass throughput. For small and medium distances from the spinneret, $\dot{\epsilon}$ increases only slightly. At the beginning of the neck, a rapid increase of the elongation rate is observed for all three take-up speeds. For an increase of the take-up speed from 4500 to 5500 m/min, the maximum of the elongation rate increases from 400 to 1400 s^{-1}.

In Figure 24, profiles of the tensile stress and the

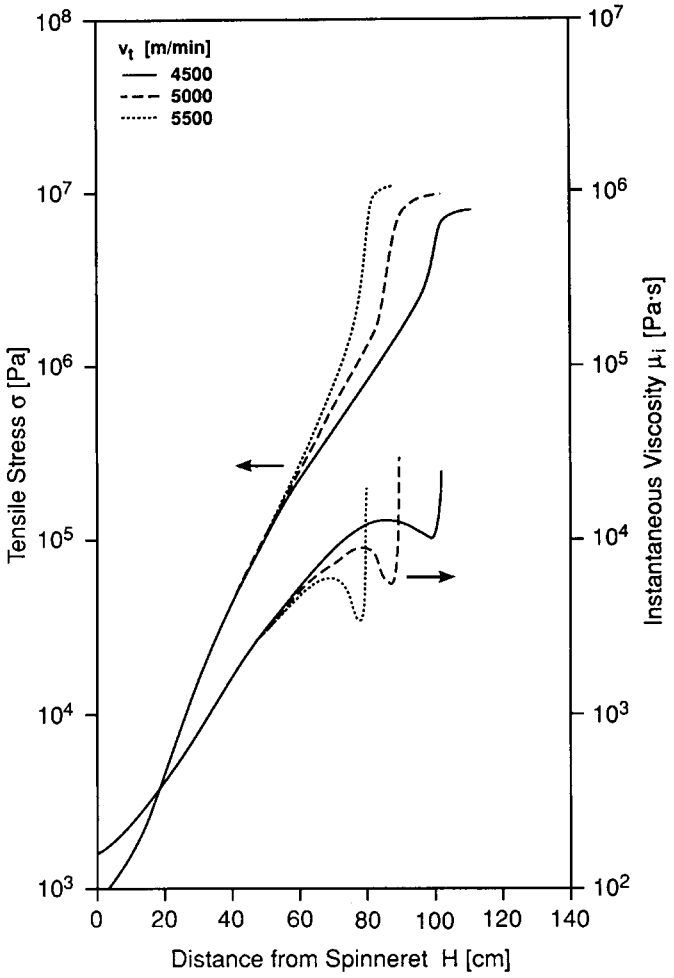

Figure 24 Profiles of the tensile stress $\sigma(H)$ and of the instantaneous elongational viscosity $\mu_i(H)$ of PA 66 filaments spun at different take-up speeds v_t. Mass throughput $\dot{m}$ = 1.86 g/min/orifice.

instantaneous elongational viscosity of PA 66 filaments, spun at three different take-up speeds, are shown. In the stress profiles, the necking is indicated by a strong increase of the tensile stress immediately before the solidification of the filaments. The further increase in tensile stress observed after solidification is caused by air drag. With increasing take-up speed, the tensile stress at the solidification point $\sigma(H_o)$ increases. Further investigations showed that, within the limits of experimental error (±10%), $\sigma(H_o)$ does not depend on any other spinning parameter, such as, for example, mass throughput or cooling rate.

At small and intermediate distances H from the spinneret, the instantaneous elongational viscosity μ_i increases with increasing H, as one would expect, due to the decrease of the filament temperature. At larger distances, this increase flattens, and μ_i passes through a maximum immediately before the onset of filament necking. Within the neck region, the instantaneous elongational viscosity even decreases with increasing H, despite the decrease in filament temperature. The onset of the crystalline solidification causes μ_i to rise sharply at the end of the neck region.

There are several possible explanations for the observed drop in the instantaneous elongational viscosity. As the present experiments showed, crystallization does not occur before the end of the neck-like deformation. This means that any explanation

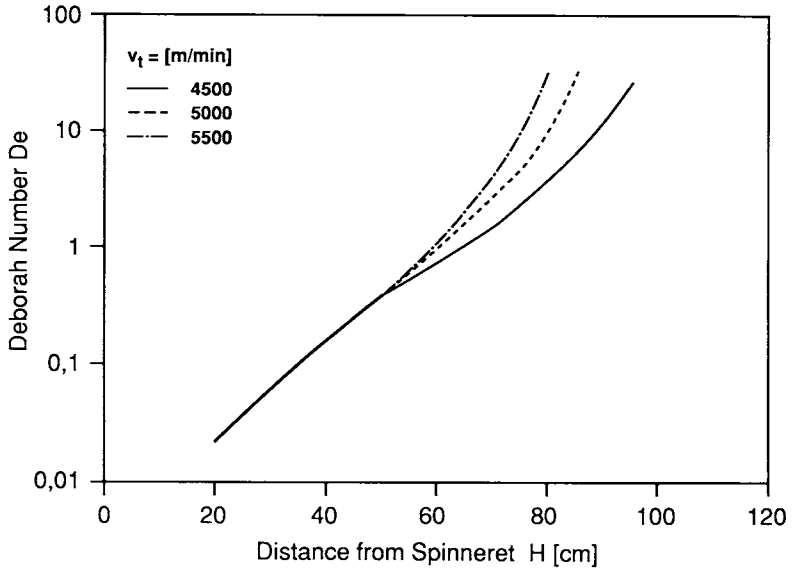

Figure 25 Development of the Deborah number $De(H)$ of PA 66 filaments spun at different take-up speeds v_t. Mass throughput $\dot{m}$ = 1.86 g/min/orifice.

can be excluded that relates the onset of the neck-like deformation to the onset of crystallization, such as, for example, a decrease of μ due to the heat released during crystallization or a spontaneous elongation upon crystallization.

For PET, evidence has been discussed in the literature about the existence of an ordered "mesophase".[34] As suggested by Shimizu et al.,[8] this mesophase could be responsible for the decrease of the elongational viscosity within the "neck" of fast spun PET. However, the present WAXS data do not provide any evidence for the existence of such a mesophase in high-speed spun polyamides.

Assuming that within the neck the melt deformation takes place under quasi-stationary conditions, the drop in the instantaneous elongational viscosity μ_i could also reflect a drop in the steady-state elongational viscosity μ. A decrease of μ could be caused by the strong increase of the strain rate immediately above the solidification point (Fig. 23). As is well-known from isothermal experiments, the elongational viscosity μ decreases at high deformation rates.[35] In order to explain the observed behavior of $\mu_i(H)$, the strain-rate-induced drop in the steady-state elongational viscosity $\mu(H)$ would have to overcompensate a rise of $\mu(H)$, caused by the decrease of the melt temperature along the spinline.

As already mentioned, this interpretation of the viscosity profile $\mu_i(H)$ is based on the assumption that the extension within the neck zone takes place in a quasi-steady state. In other words, it is assumed that changes in the elastic strain contributions (transient viscoelastic effects) are negligible. However, as discussed in the next section, it is most likely that transient viscoelastic effects cannot be neglected in the neck region occurring immediately above the solidification point. One can conclude, therefore, that the decrease of μ_i is not related to a decrease in the steady-state elongational viscosity, but is rather caused by a strong increase in the elastic (recoverable) strain contributions. According to the relation

$$\mu_i = \frac{\sigma}{\frac{\Delta\epsilon}{\Delta t}} = \frac{\sigma}{\frac{\Delta\epsilon_r}{\Delta t} + \frac{\Delta\epsilon_v}{\Delta t}} = \frac{\sigma}{\dot{\epsilon}_r + \dot{\epsilon}_v} \leqq \frac{\sigma}{\dot{\epsilon}_v} = \mu \qquad (9)$$

elastic contributions to the spinline deformation could lead to the observed drop in the instantaneous elongational viscosity. In eq. (9), $\Delta\epsilon_r$ and $\Delta\epsilon_v$ mean the Henky measure of the recoverable (elastic) and viscous contribution to the total changes in elongation $\Delta\epsilon$. From the minimum of μ_i at 5500 m/min and the value of μ_i at 4500 m/min at the same position H, one can estimate that $\dot{\epsilon}_r$ is more than 2.5 times larger than $\dot{\epsilon}_v$ in the neck region.

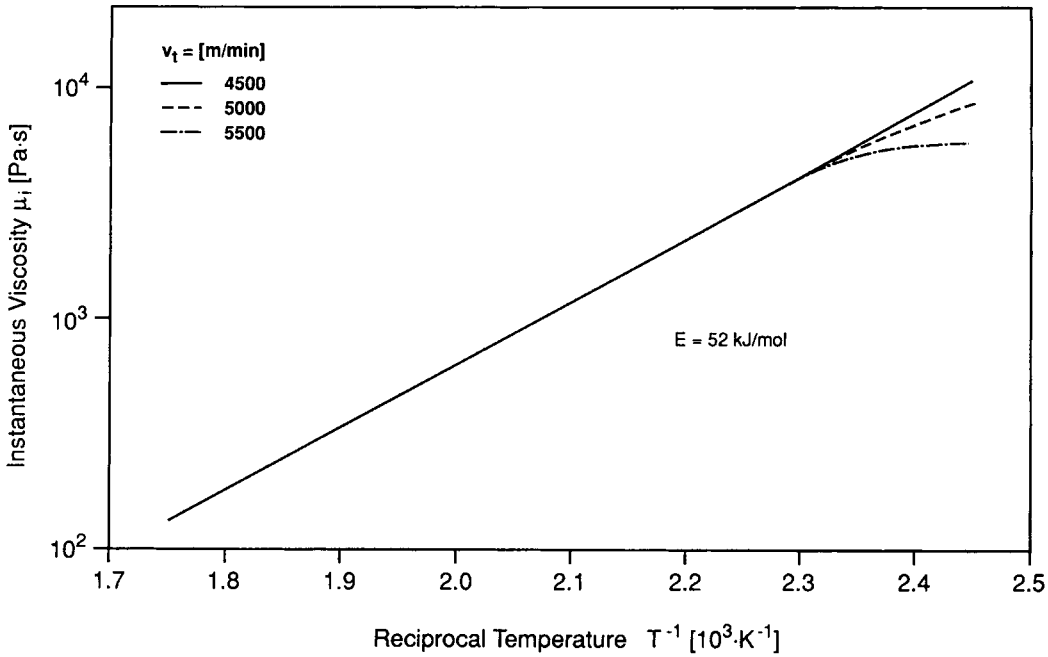

Figure 26 Arrhenius plot of the instantaneous elongational viscosity μ_i of PA 66 filaments spun at different take-up speeds v_t. Mass throughput $\dot{m}$ = 1.86 g/min/orifice.

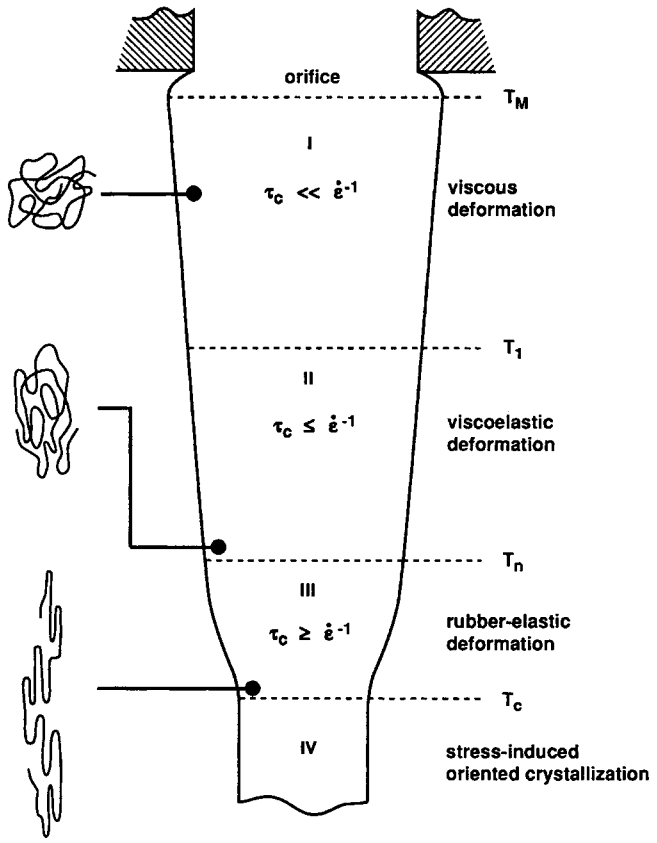

Figure 27 Schematic representation of the deformation process and the development of the molecular structure of high-speed spun polyamides along the spinline.

To our knowledge Tomka,[36] Schöne,[15] and Perez and Lecluse[1] were the first to interpret the neck-like deformation as an elastic effect. On the other hand, in a recent study of the kinematics of inertialess jets of Newtonian, Reiner–Rivlin, "power-law," and corotational Maxwell fluids, Ziabicky[37] showed that in the frame work of these models the neck-like deformation cannot be explained by elastic contributions.

Molecular Picture of Structure Development in High-Speed Spinning

For a description of the molecular processes taking place during high-speed spinning, we regard the polymer melt as a temporary network. The crosslinks of such a network consist of temporary entanglements of the chain molecules. In this picture, the molecular structure develops as a result of two competing processes: A strain process, which causes an elongation of the chain molecules and thereby a deformation of the molecular network, and a relaxation process, trying to bring back the chains into their original Gaussian conformation and thereby keeping the molecular network undeformed.

The characteristic time of the deformation is given by the reciprocal deformation rate $\dot{\epsilon}^{-1}$. Correspondingly, the relaxation process can be described by a characteristic relaxation time τ_c. Assuming that the chain relaxation takes place by chain reptation,[38] τ_c essentially describes the time needed for a chain to escape from the tube in which it is confined laterally due to its entanglements with surrounding polymer chains.

In Figure 25, the so-called Deborah number $De = \tau_c \cdot \dot{\epsilon}$[39] is plotted vs. the distance from the spinneret. τ_c was calculated according to the relation

$$\tau_c = \mu(T) \cdot D_e^o \qquad (10)$$

where $D_e^o = 3 \times 10^{-6}$ Pa^{-1} was used for the equilibrium elongational complience of PA 66.[40] At small distances from the spinneret, this means at high melt temperatures, the relaxation process proceeds much faster than the strain process ($\tau_c \ll \dot{\epsilon}$). Correspondingly, the draw down of the melt will not cause any significant elongation of the chain molecules so that they will remain in a nearly Gaussian coil conformation. This means that elastic (recoverable) effects will not play a major role in the deformation process at small distances from the spinneret. Therefore, in this region one would expect the instantaneous elongational viscosity μ_i to be identical to a good approximation with the steady-state elongational viscosity μ.

The Arrhenius plot of the viscosity data shown in Figure 26 confirms this assumption. From the slope of the straight line fitted through the "high temperature" data, an apparent activation energy $E = 52$ kJ/Mol is obtained, which is in relatively good agreement with the value $E = 60$ kJ/Mol determined from the temperature dependence of the zero shear viscosity η_o.[41] Due to the further decrease of the filament temperature and the further increase of the elongation rate (see Fig. 23), the characteristic relaxation and deformation time τ_c and $\dot{\epsilon}^{-1}$, respectively, become comparable at intermediate distances from the spinneret. For $\tau_c \sim \dot{\epsilon}^{-1}$, elastic strain contributions can no longer be neglected; the polymer chains will start to elongate causing the polymer network to deform.

In addition to the decreasing filament temperature, the increasing chain elongation will also reduce the chain mobility (the reptational mobility of a fully extended chain is zero!). Due to this self-reinforcing process, the mobility of the chains is reduced rapidly to a point where the polymer molecules can no longer respond to the applied deformational force by a disentanglement process via chain reptation. Now the temporary entanglements become permanent to a good approximation, which means that they can be looked at as crosslinks of a permanent molecular network.

As can be seen from a comparison of Figures 24 and 25, the filament necking starts for a Deborah number of about 5 for all take-up speeds investigated. Assuming that the onset of necking is caused by the immobilization of the entanglements, as is described above, the filament reduction in the neck region can be described to a good approximation as a rubber elastic deformation of the melt. At the end of the neck, the high molecular orientation caused by the rubber-elastic deformation will result in an orientation- (stress-) induced crystallization, which is typical for all polycondensates spun at sufficiently high speeds.

According to this picture, the deformation process of polyamides can roughly be divided into three regions of different rheological behavior of the melt (see Fig. 27):

Region I ($\tau_c \ll \dot{\epsilon}^{-1}$). To a good approximation the diameter reduction is caused by a purely viscous de-

formation of the melt. The average chain conformation stays undistorted to a good approximation.

Region II ($\tau_c \leq \dot{\epsilon}^{-1}$). Elastic contributions can no longer be neglected, the diameter reduction is caused by a viscoelastic deformation. The chains start to elongate.

Region III ($\tau_c > \dot{\epsilon}^{-1}$). To a good approximation, the reduction of the filament diameter in the neck region is caused by a rubber-elastic deformation of the melt. Viscous contributions to the deformation are small compared to the elastic ones. In the neck region, the average elongation of the chains increases rapidly to a final level at the end of the neck.

CONCLUSIONS

The neck-like deformation process occurring in high-speed melt spinning of PA 66 and PA 6 at take-up speeds of between 4200 and 5500 m/min was investigated by on-line laser light scattering, thermographic contrast compensation, and WAXS measurements.

At the spinning speeds applied in this investigation, both polyamides show a neck-like deformation immediately above the solidification point of the filament. The solidification takes place by a fast stress-induced oriented crystallization. To a good approximation, crystallization temperature and crystallization rate, as well as crystallinity and crystal orientation, are determined by the take-up speed only. Increasing take-up speed results in an increase of the crystallization parameters listed above. Raising the molecular mass leads to an increase of the crystallization temperature and so to a shift of the neck towards the spinneret.

At the same take-up speeds, PA 6 and PA 66 have similar crystallization temperatures, but different crystallization rates. PA 66 crystallizes faster than PA 6. In the range of take-up speeds applied, upper limits of the crystallization half times were found to be 0.3 to 0.6 ms for PA 66 and 0.6 to 1 ms for PA 6.

By measuring simultaneously diameter and temperature profiles in the neighborhood of the neck, it was found that crystallization takes place at the end of the neck. Consequently, the formation of the neck is not primarily caused by the onset of crystallization. This means that the neck-like deformation can be explained neither by a reduction of the elongational viscosity due to the heat of crystallization nor by a spontaneous elongation upon crystallization.

From a detailed discussion of the profiles of the tensile stress and the instantaneous elongational viscosity, it is concluded that to a good approximation, the neck is caused by a rubber-elastic deformation of the melt. A simple picture of the deformation process of polyamides melt-spun at high speeds is given. In this picture, three regions of different rheological behavior of the melt along the spin line are distinguished with increasing distance from the spinneret: Region I, in which a purely viscous deformation of the melt stream dominates, region II, with a viscoelastic deformation, and region III (neck-region), where the reduction of the diameter is primarily caused by a rubber-elastic deformation.

The authors thank Dr. K. Weinerth, Dipl.-Ing. A. Weher, and Dipl.-Ing. H. W. Rillig for their valuable support on high-speed spinning and Drs. H. M. Laun and H. Schuch for stimulating discussions. We also thank our coworkers, H. Baumann, Mrs. H. Hübner, D. Lummel, and F. Magin, for their committed cooperation on performing and evaluating the on-line experiments.

REFERENCES

1. G. Perez and C. Lecluse, *Proc. 18th Int. Man-Made Fibre Conf.*, Dornbirn, Austria, June 20–22, 1979.
2. H. H. George, *A Study of Structural Development in the High-Speed Spinning of Poly(Ethylene Terephthalate)*, presented at Gordon Conference "Fiber Science," New London, NH, July 4, 1980.
3. J. Shimizu, *Conf. High-Speed Spinning*, Osaka, Japan, Dec. 9–10, 1981.
4. M. Matsui, *Conf. High-Speed Spinning*, Osaka, Japan, Dec. 9–10, 1981.
5. W. Dietrich, G. Reichelt, and H. Renkert, *Chemiefasern Textilind.*, **32**, 612 (1982).
6. H. H. George, A. Holt, and A. Buckley, *Polym. Eng. Sci.*, **23**, 95 (1983).
7. M. Matsui, in *High-Speed Fiber Spinning*, A. Ziabicki and H. Kawai, Eds., Wiley–Interscience, New York, 1985.
8. J. Shimizu, N. Okui, and T. Kikutani, in *High-Speed Fiber Spinning*, A. Ziabicki and H. Kawai, Eds., Wiley–Interscience, New York, 1985.
9. H. H. George, in *High-Speed Fiber Spinning*, A. Ziabicki and H. Kawai, Eds., Wiley–Interscience, New York, 1985.
10. G. Perez, in *High-Speed Fiber Spinning*, A. Ziabicki and H. Kawai, Eds., Wiley–Interscience, New York, 1985.
11. S. Chen, W. Yu, and J. E. Spruiell, *J. Appl. Polym. Sci.*, **34**, 1477 (1987).

12. Fu-Min Lu and J. E. Spruiell, *J. Appl. Polym. Sci.*, **34,** 1541 (1987).
13. K. F. Zieminski and J. E. Spruiell, *J. Appl. Polym. Sci.*, **35,** 2223 (1988).
14. J. H. Bheda and J. E. Spruiell, *J. Appl. Polym. Sci.*, **39,** 447 (1990).
15. A. Schöne, *Chemicke Vlakna (CSRS)*, **32,** 25 (1982).
16. K. I. Katayama and M. G. Yoon, in *High-Speed Fiber Spinning,* A. Ziabicki and H. Kawai, Eds., Wiley–Interscience, New York, 1985.
17. R. M. Patel, J. H. Bheda, and J. E. Spruiell, *J. Appl. Polym. Sci.*, **42,** 1671 (1991).
18. H. Breuer, *Internal BASF Report,* 1984.
19. K. Hahn, *Internal BASF Report,* 1984.
20. D. Rhoner, *Melliand Textilberichte,* **63,** 117 (1982).
21. H. H. George, *Polym. Eng. Sci.*, **22,** 292 (1982).
22. S. Kase and T. Matsuo, *J. Appl. Polym. Sci.*, **11,** 251 (1967).
23. C. Lecluse, *Conf. Nylon: Retrospect and Prospect,* University of Leeds, July 5–7, 1983.
24. H. M. Heuvel and R. R. Huisman, in *High-Speed Fiber Spinning,* A. Ziabicky and H. Kawai, Eds., Wiley–Interscience, New York, 1985.
25. K. Koyama, J. Suryadevara, and J. E. Spruiell, *J. Appl. Polym. Sci.*, **31,** 2203 (1986).
26. A. Ziabicky, *Fundamentals of Fibre Formation,* Wiley, London, 1976.
27. A. Ziabicki and L. Jarecki, in *High-Speed Fiber Spinning,* A. Ziabicki and H. Kawai, Eds., Wiley–Interscience, New York, 1985.
28. F. S. Smith and R. D. Steward, *Polymer,* **15,** 283 (1974).
29. G. C. Alfonso and M. P. Verdona, *Polymer,* **19,** 711 (1978).
30. G. Althen and H. G. Zachmann, *Makromol. Chem.*, **180,** 2723 (1979).
31. H. Janeschitz-Kriegl, *Polymer Melt Rheology and Flow Birefringence, Polymers/Properties and Applications 6,* J. Meißner, Ed., Springer–Verlag, Berling, Heidelberg, New York, 1983.
32. G. Vassilatos, B. H. Knox, and H. R. E. Frankfort, in *High-Speed Fiber Spinning,* A. Ziabicki and H. Kawai, Eds., Wiley–Interscience, New York, 1985.
33. H. M. Laun, *Internal BASF Report,* 1979.
34. M. Sotten, A. M. Arniaud, and C. Rabourin, *J. Appl. Polym. Sci.*, **22,** 2585 (1978).
35. H. M. Laun and H. Schuch, *J. Rheology,* **33,** 119 (1989).
36. J. C. Tomka, *Conf. Nylon: Retrospect and Prospect,* University of Leeds, July 5–7, 1983.
37. A. Ziabicki, *J. Non-Newt. Fl. Mech.*, **30,** 141 (1988).
38. P. G. de Gennes, *Scaling Concepts in Polymer Physics,* Cornell University, Ithaca and London, 1979.
39. R. B. Bird, R. C. Armstrong, and O. Hassager, *Dynamics of Polymer Liquids,* Vol. 1, 2nd. Ed., Wiley, New York, 1987.
40. H. M. Laun, Private Communication.
41. H. M. Laun, *Rheol. Acta,* **18,** 478 (1979).

Received March 6, 1992
Accepted April 28, 1992